The Astrophysical Journal, 707:1098–1114, 2009 December 20 doi:10.1088/0004-637X/707/2/1098

HUBBLE SPACE TELESCOPE OPTICAL IMAGING OF THE ERODING DEBRIS DISK HD 61005

H. L. Maness[1], P. Kalas[1], K. M. G. Peek[1], E. I. Chiang[1], K. Scherer[2], M. P. Fitzgerald[3], James R. Graham[1], D. C. Hines[4],
G. Schneider[5], and S. A. Metchev[6]
[1] Department of Astronomy, University of California at Berkeley, Berkeley, CA 94720, USA
[2] Institut für Theoretische Physik IV, Ruhr Universität Bochum, 44780 Bochum, Germany
[3] Lawrence Livermore National Laboratory, Livermore, CA 94550, USA
[4] Space Science Institute, Boulder, CO 80301, USA
[5] Steward Observatory, University of Arizona, Tucson, AZ 85721, USA
[6] Department of Physics and Astronomy, State University of New York - Stony Brook, Stony Brook, NY 11794, USA
Received 2009 April 14; accepted 2009 October 28; published 2009 December 2

ABSTRACT

We present *Hubble Space Telescope* optical coronagraphic polarization imaging observations of the dusty debris disk HD 61005. The scattered light intensity image and polarization structure reveal a highly inclined disk with a clear asymmetric, swept back component, suggestive of significant interaction with the ambient interstellar medium (ISM). The combination of our new data with the published 1.1 μm discovery image shows that the grains are blue scattering with no strong color gradient as a function of radius, implying predominantly submicron-sized grains. We investigate possible explanations that could account for the observed swept back, asymmetric morphology. Previous work has suggested that HD 61005 may be interacting with a cold, unusually dense interstellar cloud. However, limits on the intervening interstellar gas column density from an optical spectrum of HD 61005 in the Na I D lines render this possibility unlikely. Instead, HD 61005 may be embedded in a more typical warm, low-density cloud that introduces secular perturbations to dust grain orbits. This mechanism can significantly distort the ensemble disk structure within a typical cloud crossing time. For a counterintuitive relative flow direction—parallel to the disk midplane—we find that the structures generated by these distortions can very roughly approximate the HD 61005 morphology. Future observational studies constraining the direction of the relative ISM flow will thus provide an important constraint for future modeling. Independent of the interpretation for HD 61005, we expect that interstellar gas drag likely plays a role in producing asymmetries observed in other debris disk systems, such as HD 15115 and δ Velorum.

Key words: circumstellar matter – planetary systems: formation – planetary systems: protoplanetary disks – stars: individual (HD 61005)

1. INTRODUCTION

Nearly two dozen dusty debris disks surrounding nearby stars have now been spatially resolved at one or more wavelengths. Many of these systems show clear similarities. For example, the radial architecture of several debris disks can be understood in terms of a unified model of steady-state dust production via collisions in a parent planetesimal belt (e.g., Strubbe & Chiang 2006). However, while the observed structure of many systems is ring-like (Kalas et al. 2006; Wyatt 2008), most disks show substructure such as clumps, warps, offsets, and brightness asymmetries not explained in traditional steady-state collisional grinding models.

These unexpected features have triggered a great deal of recent theoretical work. The effects of massive planetesimal collisions, sandblasting by interstellar grains, close stellar flybys, dust avalanches, and secular and resonant perturbations by exoplanets have all been invoked to explain the observations (e.g., Moro-Martin et al. 2008, and references therein). However, as many of these theories produce similar structures, further observational constraints are needed to better understand the key forces affecting disk structure and the circumstances in which they apply.

At a heliocentric distance of 34.5 pc (Perryman et al. 1997), the debris disk surrounding HD 61005 (SpT: G8 V; Gray et al. 2006) is a promising target for advancing our understanding in this area. The significant infrared excess for this source ($L_{\rm IR}/L_* = 2 \times 10^{-3}$) was recently discovered as part of the Spitzer FEPS survey (Carpenter et al. 2009), indicating 60 K blackbody-emitting grains $\gtrsim$16 AU from the star. Follow-up *Hubble Space Telescope* (*HST*) coronagraphic imaging observations with the Near-Infrared Camera and Multi-Object Spectrometer (NICMOS; *HST*/GO program 10527; PI: D. Hines) resolved the source (Hines et al. 2007, hereafter H07), revealing an unprecedented swept, asymmetric morphology, suggestive of significant interaction with the interstellar medium (ISM). H07 suggested that this system could be a highly inclined debris disk, undergoing ram pressure stripping by the ambient ISM. However, this interpretation requires an unusually high interstellar density for the low-density Local Bubble in which HD 61005 resides. Furthermore, the single wavelength intensity image was insufficient to provide strong constraints on the dominant size of the scattering grains and the overall scattering geometry.

To further quantify the physical properties of grains seen in scattered light and the overall geometry of the system, we obtained optical coronagraphic polarimetry imaging observations of HD 61005 with the Advanced Camera for Surveys (ACS) onboard *HST*. As demonstrated by Graham et al. (2007) for the case of AU Mic, polarization observations in scattered light are invaluable for breaking degeneracies between grain scattering properties and their spatial distribution. Furthermore, the ACS data represent a factor of 2 improvement in angular resolution compared to the 1.1 μm discovery observations. In addition to these new imaging data, we also obtained a high-resolution optical spectrum to characterize ambient interstellar gas surrounding this system. In Section 2, we describe the steps taken in observing and reducing these data. In Section 3, we discuss the results of these observations, their consequences for the system scattering geometry, and the additional constraints they provide when combined with the 1.1 μm NICMOS image. In Section 4, we explore whether interactions with ambient interstellar gas can plausibly explain the observed swept, asymmetric morphology in this system. We discuss the implications for these potential explanations in Section 5 and summarize our findings in Section 6.

2. OBSERVATIONS AND DATA REDUCTION

We obtained optical coronagraphic observations of HD 61005 using the ACS high-resolution camera (HRC) $1\farcs8$ diameter occulting spot on 2006 December 19 (*HST*/GO program 10847; PI: D. Hines). In each of two contiguous orbits, we imaged HD 61005 with the F606W filter in combination with the POL0V, POL60V, and POL120V polarizer filters (two 340 s exposures per filter combination). Aside from the telescope position angle (P.A.), which is rotated $23\fdg032$ between orbits, the observational procedures for the two HD 61005 orbits were identical. Before the HD 61005 orbits, we observed the point-spread function (PSF) reference star HD 82943 (SpT: F9 V; Gray et al. 2006; $B = 7.16$, $V = 6.56$) using an observing sequence identical to the two orbits allocated to HD 61005 ($B = 8.93$, $V = 8.22$). We also observed a second PSF star, HD 117176 (SpT: G5 V; Gray et al. 2001; $B = 5.69$, $V = 5.00$), in an identical manner following the HD 61005 orbits.

For each filter combination, we combined the two 340 s, pipeline processed (bias subtracted, flat-fielded) frames by excluding the maximum value at each pixel position, thereby minimizing the impact of cosmic ray events. After dividing by the cumulative integration time of each frame, we performed sky subtraction by taking the median value in a 10×20 pixel box in the lower-left corner of the chip, which is the position farthest from the bright target star. We registered the images by selecting a fiducial HD 61005 image (the POL0V image in the first orbit) and subtracting all other HD 61005 frames using small offsets (0.02 pixels) to minimize the residuals in regions dominated by light from the stellar PSF. The offsets that minimize residual differences between frames were then applied to the individual POL0V, POL60V, and POL120V images to align them to a common reference frame relative to the star. We carried out an identical registration procedure for the two PSF reference stars.

We then subtracted the HD 61005 PSF in each of the three POL0V, POL60V, and POL120V frames by the corresponding frames from each of the two PSF reference stars. Prior to subtraction, we scaled each reference star to match the expected brightness of HD 61005, using photometry obtained from the direct images. The HD 117176 observations, made immediately following the HD 61005 orbits yielded a better subtraction than the HD 82943 observations, made five weeks prior to the HD 61005 orbits. We therefore used the subtraction obtained with HD 117176 for all subsequent analysis.

Following PSF subtraction, we corrected the resultant images for geometric distortion yielding 25 mas × 25 mas pixels. We then constructed Stokes parameter images corrected for instrumental polarization following Pavlovsky (2006). For the ACS/HRC/F606W/POLV instrumental configuration and high fractional linear polarization ($p = (Q^2 + U^2)^{1/2}/I \geqslant 0.2$), the residual systematic error is 10% of the computed polarization fraction. For less strongly polarized sources ($p < 0.2$), the systematic error in the degree of linear polarization is approximately constant at $\sigma_p = 0.01$. In both cases, the systematic uncertainty in the P.A. is 3°.

We next calculated polarization vectors from the derived Stokes images. As the polarization fraction is intrinsically positive and biased upward by noise, we employed the spatial binning algorithm of Cappellari & Copin (2003) to bin the Stokes I, Q, and U images to approximately constant signal to noise prior to this calculation. Within $\sim 1\farcs4$ of the star, the computed polarization vectors become significantly disordered in magnitude and direction, as a result of systematic PSF subtraction errors. We therefore only consider polarization vectors outside this radius in our analysis. The surface brightness at $0\farcs9$–$1\farcs4$ is similarly compromised and should be treated with caution.

Finally, we converted from instrumental to physical brightness units using the synthetic photometry package, Synphot. As input, Synphot requires the instrument configuration (camera, coronagraph, wideband, and polarizing filters) and the source spectrum across the band. Since the latter is unknown, we performed the calculations three times assuming: (1) a flat spectrum, (2) a $T_{\rm eff} = 5500$ K Kurucz synthetic spectrum approximating the G-dwarf stellar spectrum, and (3) a spectral slope across each band that is the same as that calculated between the NICMOS and ACS bands using method (2). All methods yielded conversion factors within 1% of each other, suggesting the assumed source spectrum factors negligibly into the total color uncertainties.

In addition to the ACS observations, we analyze two additional data sets: (1) the NICMOS F110W image; a full description of the NICMOS data acquisition and reduction is given in H07; and (2) high-resolution ($R \approx 60{,}000$) echelle spectra for HD 61005 and two comparison stars of similar spectral type (HD 33822: $T_{\rm eff} = 5850$ K, HD 13836: $T_{\rm eff} = 5580$ K; Masana et al. 2006). The spectra were obtained on the Keck I telescope with the HIRES spectrometer on 2004 December 30, 2006 January 16, and 2008 November 9. The wavelength range was 3700–6200 Å, though our analysis concerns only the Na I D lines at 5889.951 Å and 5895.924 Å. We used a standard procedure to perform flat-fielding, sky subtraction, order extraction, and wavelength calibration of the raw echelle images (Butler et al. 1996; Vogt et al. 1994).

3. RESULTS

3.1. ACS Scattered Light and Polarization

3.1.1. Two-dimensional Morphology and Polarization Structure

Figures 1 and 2 display the F606W total intensity image of HD 61005 on a logarithmic and linear scale, respectively. The figures show two distinct morphological components. The first component, denoted by NE1 and SW1 in Figure 2, resembles a near edge-on disk. The putative midplane for this component is observed to extend out to $\sim 3''$ from the star, where the signal to noise per pixel falls below unity. The second morphological component is detected below the nominal disk midplane. This component exhibits an asymmetric, "swept back" morphology, suggestive of significant interaction with the ISM. This unusual structure was first noted by H07 in their NICMOS F110W discovery image. Both the disk-like and swept-back components additionally exhibit a striking asymmetry between the northeast and southwest sides of the source. At a given projected radius, the northeast side of the source is approximately twice as bright as the southwest side. This brightness asymmetry is also seen in the NICMOS F110W image (e.g., H07, Figure 4).

Figure 3 displays the polarized flux of image of HD 61005, while Figure 1 overplots polarization vectors on the Stokes I

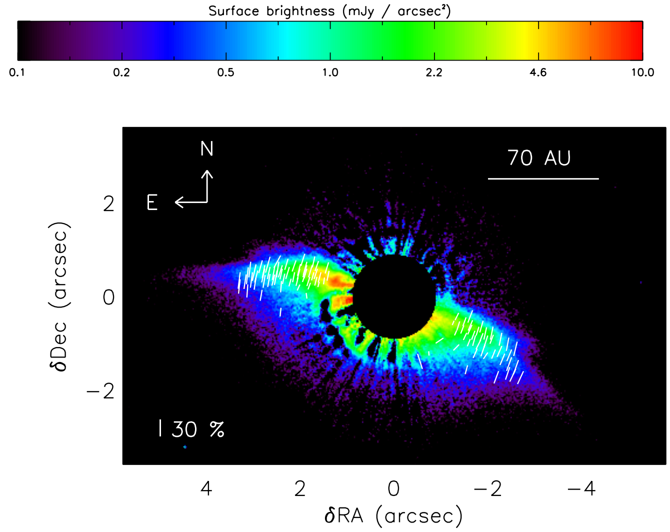

Figure 1. Logarithmically scaled image of HD 61005 in Stokes I at $\geqslant 0.1$ mJy arcsec^{-2} with polarization vectors and a 1″.8 coronagraphic mask overplotted. The color bar units were calculated using the synthetic photometry package, Synphot. The plotted polarization vectors were computed from Stokes images binned to approximately constant signal to noise.

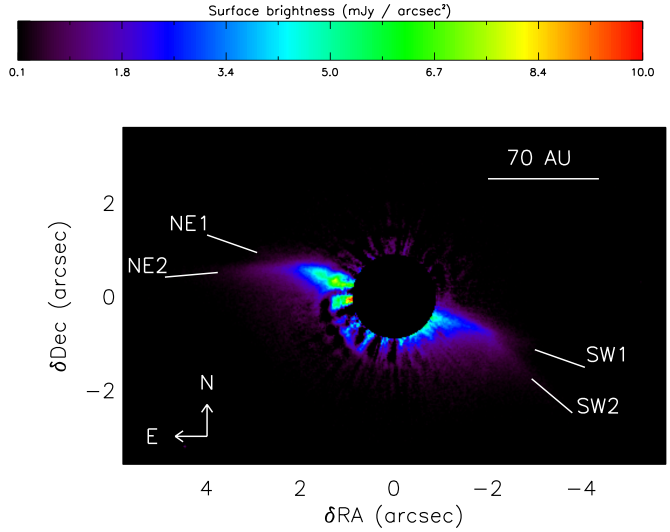

Figure 2. Same as Figure 1, only with a linear display scale and without polarization vectors. Overplotted are labels for the surface brightness components displayed in Figure 5.

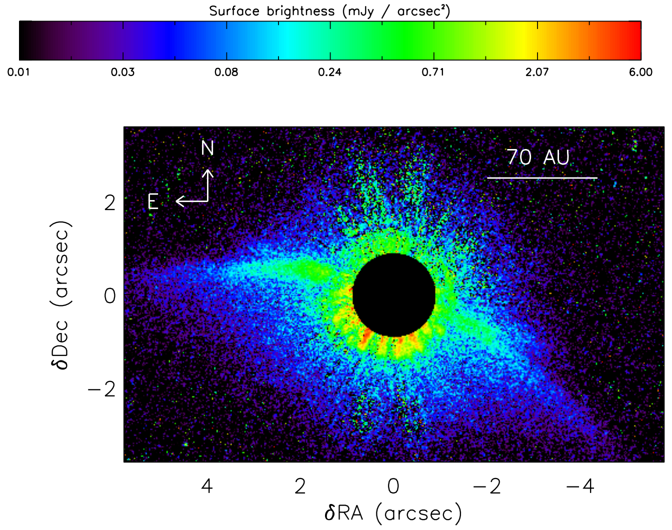

Figure 3. Logarithmically scaled polarized flux ($\sqrt{Q^2+U^2}$) image of HD 61005.

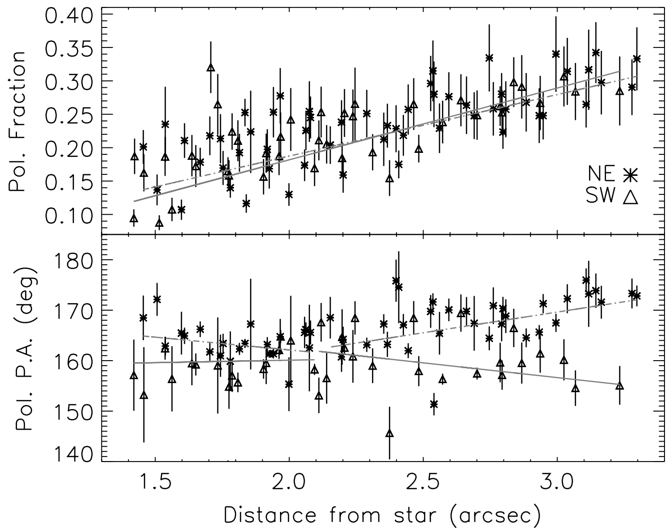

Figure 4. One-dimensional version of the binned polarization vectors displayed in Figure 1. In the top panel, the data show a clear increase in fractional polarization with distance from the star. Linear fits to the data are overplotted in gray with a solid line for the southwest side and a dot-dashed line for the northeast side. In the bottom panel, the rotation of the electric field orientation in the swept back outer disk is seen in the deviation from the nominal midplane polarization P.A. outside ∼2″.1. Linear fits for data in and outside this radial distance are overplotted.

image, spatially binned according to the procedure outlined in Section 2. The polarization vectors in Figure 1 show that along the plane of the disk, the fractional polarization increases with radial distance from the star from ∼10% to ∼35%. The orientation of the electric field within ∼2″.1 also appears perpendicular to the nominal disk midplane. In the swept-back area of the source, the polarization vectors rotate to become approximately perpendicular to the outer edge of this component. The fractional polarization in this region is similar to that seen in the outer part of the disk component.

3.1.2. Disk Component Parameters

The ACS polarization results add further evidence to the suggestion by H07 that HD 61005 is a near edge-on debris disk. In particular, the HD 61005 polarization structure is very similar to that seen in the spectrally blue edge-on debris disk around the M dwarf, AU Mic, observed using the same instrumental configuration (Graham et al. 2007). The midplanes of both HD 61005 and AU Mic exhibit high fractional polarization ($p_{\max} \sim 0.4$) which increases with projected radius. Similarly, both disks exhibit an electric field orientation perpendicular to the disk midplane at all projected radii. These features are expected for small-particle ($x \lesssim 1$) scattering in an edge-on disk (Kruegel 2003).

For HD 61005, these effects are quantified in Figure 4, which shows the binned polarization vector P.A. and magnitudes from Figure 1. Linear fits to the one-dimensional polarization P.A. versus projected distance within 2″.1 imply flat slopes, as expected for a highly inclined disk geometry (-5.1 ± 2.5 and 1.0 ± 3.3 for the northeast and southwest sides, respectively). Averaging all polarization position angles within 2″.1, the implied disk P.A. is 71.7 ± 0.7 deg, where the listed uncertainty

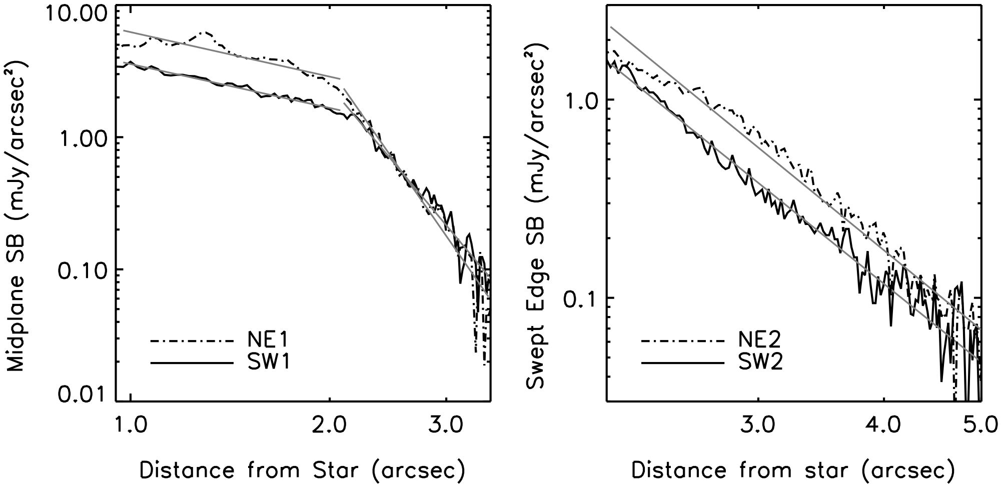

Figure 5. Surface brightness profiles through the disk midplane (left) and the outer edge of the swept back component (right). The cuts are one pixel wide, and the components listed in the legends are labeled in Figure 2. The directions for the cuts are taken from the P.A. derived in Sections 3.1.2 and 3.1.3. The power-law fits described in the text are overplotted in gray. The data show a pronounced brightness asymmetry between the northeast and southwest disk lobes.

is purely statistical and does not include the additional 3° calibration uncertainty (Section 2). The steady increase in polarization fraction with projected radius is also seen in Figure 4. Linear fits to the binned polarization fraction over the full extent of the source imply slopes of 0.09 ± 0.01 and 0.11 ± 0.01 for the northeast and southwest disk sides, respectively.

As an independent check on our disk interpretation, we fit elliptical isophotes to the total intensity image from Figures 1 and 2, assuming a circularly symmetric disk viewed in projection. We independently fit eight isophotes outside 1$''$.4 for $I > 1.3$ mJy arcsec^{-2}. The implied disk P.A. from these fits is 70.7 ± 0.5 deg, in good agreement with the P.A. inferred from the electric field orientation within 2$''$.1. The implied inclination to the line of sight from these fits is $i = 80.3 \pm 0.6$ deg.

3.1.3. Swept Component Parameters

The disk structure described above contrasts with previously imaged presumed interstellar dust phenomena, such as the infrared bow structure surrounding the A star δ Velorum (Gáspár et al. 2008) and the filamentary cirrus surrounding some Vega-like stars with significant infrared excess (Kalas et al. 2002). Nevertheless, Figures 1 and 2 clearly reveal a second asymmetric component of the source not typical of nearby debris disks and suggestive of interaction with the ISM.

The polarization signature of this component is evident in the systematic rotation of the polarization vectors outside ~2$''$.1. Linear fits to the one-dimensional polarization P.A. versus projected distance (Figure 4) give non-zero slopes of 8.2 ± 1.0 for the northeast lobe −5.8 ± 1.9 for the southwest lobe. Estimates for the P.A. of the outer edge of this component (cuts NE2 and SW2 in Figure 2) are obtained from the outermost polarization vector P.A. The implied P.A. for component NE2 is 82.8 ± 2.1 deg; the result for SW2 is 65.1 ± 3.8 deg.

3.1.4. One-dimensional Surface Brightness Profiles

One-dimensional surface brightness profiles through the disk midplane (components NE1 and SW1 in Figure 2; P.A. = 70°.7) and along the swept component outer edge (components NE2 and SW2 in Figure 2; P.A. = 82°.8, 65°.1) are shown in Figure 5. The midplane surface brightness follows a broken power law. The fitted power-law indices between 0$''$.9 and 2$''$.1 are −1.1 ± 0.1 for both midplane disk lobes. Between 2$''$.1 and 3$''$.5, power-law fits give indices of −7.2 ± 0.3 for component NE1 and −6.0 ± 0.2 for component SW1. Breaks in the scattered-light surface brightness of debris disks are often taken as the location of the parent body population for the scattering grains (e.g., Strubbe & Chiang 2006). However, as the midplane break approximately coincides with the position at which the outer edge of the swept component intersects the disk, this standard interpretation may not hold for this case.

The surface brightness profile for the outer edge of the swept component is well represented by a single power law (Figure 5). The fitted power-law index is −4.1 ± 0.1 for both NE2 and SW2. The listed errors for the power-law fits in this section are formal fitting errors and should be treated as lower limits to the true uncertainties.

3.2. ACS+NICMOS

3.2.1. Disk Scattered Light Colors

We computed the color of the disk by rebinning the ACS Stokes I image to the same pixel resolution as the NICMOS image (0$''$.0759). We then convolved the binned ACS image with a coronagraphically unocculted field star (the approximate NICMOS PSF) and performed the corresponding operation on the NICMOS image. Finally, we divided each image by the stellar flux density of HD 61005 at the appropriate band-center effective wavelength before dividing the NICMOS image by the ACS image.

Figure 6 illustrates that the HD 61005 debris disk appears predominantly blue with no significant systematic color gradient. The mean intensity ratio inferred from Figure 6 is 0.32 ± 0.10 (corresponding to a color index of [F606W]−[F110W] = −1.2 ± 0.3), where the error is dominated by uncertainties in the PSF subtraction. Although comparing images of different resolution can result in systematic color errors (e.g., Golimowski et al. 2006), our convolution steps appear to have a small effect; the mean color neglecting convolution is within 1σ of that found including convolution.

The blue color inferred from Figure 6 (ratio < 1) is rare, as the handful of debris disks with color measurements to date show mainly red colors (Meyer et al. 2007, and references therein). There are several notable exceptions, however. The

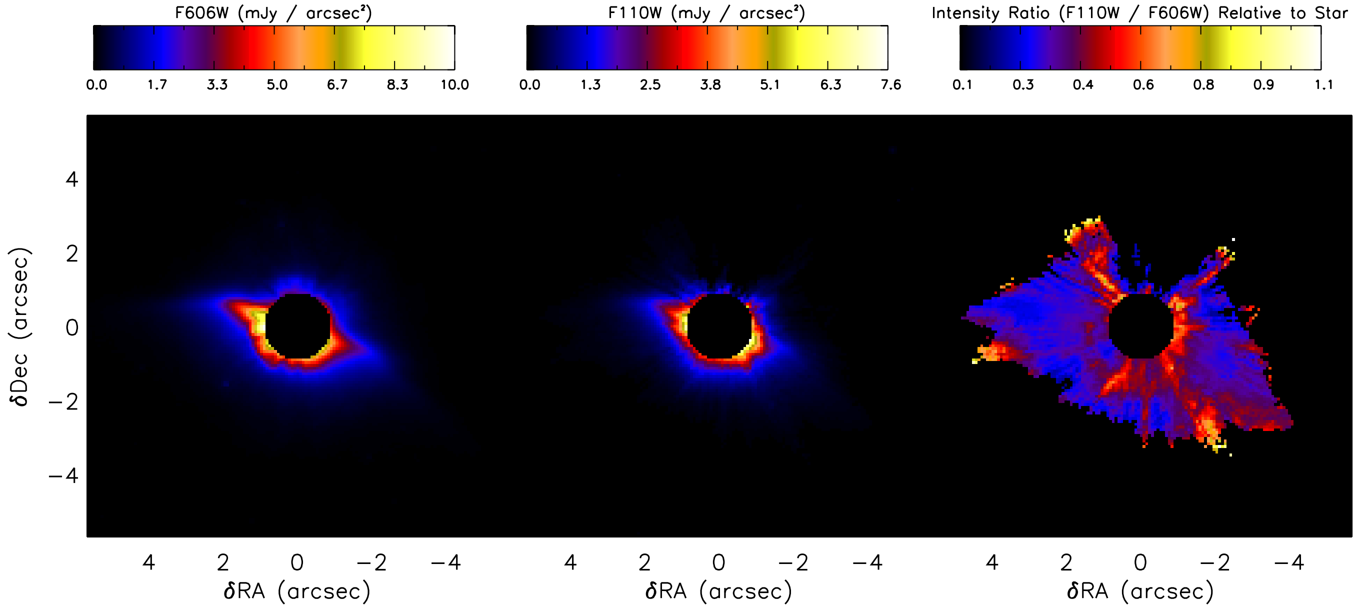

Figure 6. ACS and NICMOS images processed to compute the grain color. The left panel displays the ACS image binned to the NICMOS pixel resolution and convolved with the NICMOS off-spot PSF. The middle panel displays the NICMOS image convolved with the ACS PSF. The right panel shows a masked ratio image of the left and middle images divided by the stellar flux density ratio; values less than unity represent grains that preferentially scatter blue light, whereas values greater than unity represent grains that preferentially scatter red light. In the ratio image, we have applied a mask to all pixels with values less than 2.5 times the background level in either original image. The ratio image indicates that the disk appears predominantly blue with no appreciable color gradient.

HD 32297 and HD 15115 debris disks, for example, have been suggested to show blue optical to near-infrared scattered light colors (Kalas 2005; Kalas et al. 2007), though the result for HD 32297 is currently under debate (Debes et al. 2009). Interestingly, both disks have morphological features consistent with ISM interaction. HD 32297 shows a bowed disk structure, similar to HD 61005, though on a much larger scale (∼1000 AU; Kalas 2005). HD 15115 is highly asymmetric, perhaps as the result of ISM erosion (Debes et al. 2009).

The M dwarf debris disk, AU Mic, which has a similar polarization structure to HD 61005 (Section 3.1.2), also shows blue optical to near-infrared colors, with a color gradient toward bluer colors at larger radial distances, indicating changes in the grain size distribution (Strubbe & Chiang 2006; Fitzgerald et al. 2007). The global [F606W]−[F110W] color of the HD 61005 disk is comparable to the [F606W]−J AU Mic disk color at projected radii within ∼40 AU, the approximate location of the parent body ring in this system (Fitzgerald et al. 2007).

Like AU Mic, the blue color of the HD 61005 disk is likely due to the disk grain size distribution. Scattered light images afford a relatively narrow window on the grain size population because the brightness at a given location in the disk is largely determined by the product of the grain size distribution and the grain scattering cross section. In the presence of a steep size spectrum characteristic of a collisional cascade, this product is strongly peaked near $x \equiv \frac{2\pi a}{\lambda} \sim 1$. For example, for the Dohnanyi spectrum with $dn/da \propto a^{-7/2}$ (Dohnanyi 1969), this peak occurs at $x \simeq 2$–6, depending on the optical properties of the grain material. In Figure 7, a Mie calculation shows the peak for water ice and astronomical silicates at 0.6 μm and 1.1 μm as a function of grain size. The plots illustrate that the HD 61005 NICMOS images trace grains with radii of order 0.2–2 μm, while the ACS images trace systematically smaller grains with radii of order 0.1–1 μm. Thus, the observation that HD 61005 is globally brighter at optical wavelengths than near-infrared wavelengths suggests the disk contains a larger number of grains at increasingly small sizes, consistent with our expectation of a steep size spectrum.

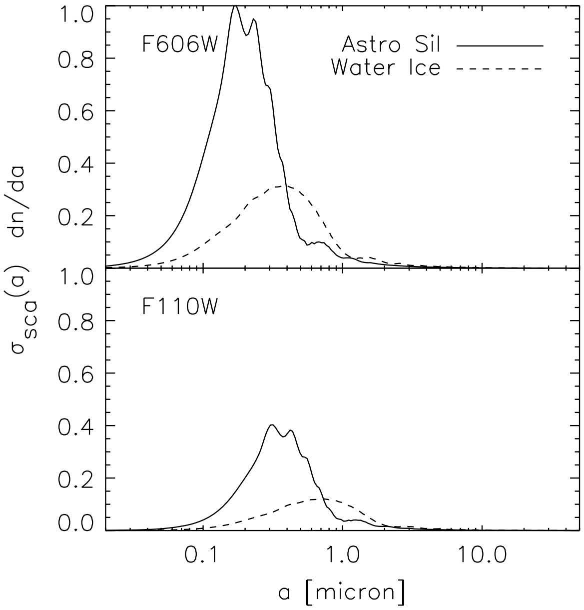

Figure 7. Product of the scattering cross section and a Dohnanyi size spectrum as a function of logarithmic grains radius for spherical particles. At a given wavelength, this product largely determines the surface brightness at a particular location in the disk. Assuming a steep size spectrum (e.g., Dohnanyi), a large peak is observed near $x \sim 1$. Thus a given scattered light image traces a relatively narrow window of the grain size population. The HD 61005 disk is globally brighter at optical wavelengths than near-infrared wavelengths, likely reflecting the larger number of grains at increasingly small sizes. The above results are monochromatic: $\lambda_{\mathrm{F606W}} = 0.6$ μm and $\lambda_{\mathrm{F110W}} = 1.1$ μm.

The inference that the F606W ACS images trace predominantly submicron-sized grains is also consistent with the imaging polarimetry results (Section 3.1). The large polarization

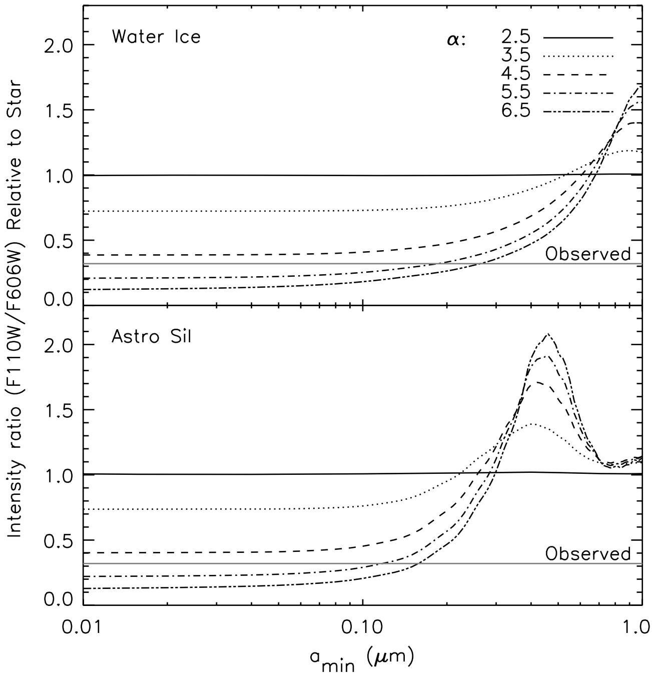

Figure 8. Implied disk colors for ice and silicate grains for grain size distributions of the form: $dn/da \propto a^{-\alpha}$, where $a_{\rm min} < a < 1$ mm. The data place an upper limit on the minimum grain size ($a_{\rm min} \lesssim 0.3$ μm) and suggest a global size distribution steeper than the canonical Dohnanyi size spectrum ($\alpha = 3.5$).

fraction and electric field orientation perpendicular to the edge-on midplane are in qualitative agreement with the expected signature of scattering by small spherical particles with $x \lesssim 1$ (Kruegel 2003). For larger spherical grains, the electric field orientation can rotate by 90° at certain scattering angles, resulting in an orientation parallel to the edge-on midplane. Furthermore, any line of sight comprising emission from a range of scattering angles will tend to show weak linear polarization (Graham et al. 2007). Neither of these features is consistent with the HD 61005 polarization results.

By integrating the curves in Figure 7 and comparing the results to the measured color, we can constrain the size distribution. The results of this procedure are shown in Figure 8, which shows the implied color for ice and silicate grains for grain size distributions of the form: $dn/da \propto a^{-\alpha}$, where $a_{\rm min} < a < 1$ mm. A range of minimum grain sizes are considered, as radiation pressure could potentially remove a fraction of small grains from the system (Appendix A). The data place an upper limit on the minimum grain size: $a_{\rm min} \lesssim 0.3$ μm. Figure 8 also suggests that the global size distribution is steeper than the Dohnanyi spectrum: $\alpha \sim 4.5$–5.5. This slope is consistent with results from collisional equilibrium modeling of other debris disk systems (e.g., Strubbe & Chiang 2006). However, the applicability of these models to the unique HD 61005 system is presently uncertain.

3.2.2. Astrometric Test for Low-mass Companions

The ACS and NICMOS images contain four field stars in common to both data sets, roughly offset from HD 61005 in R.A. and decl. by $[-2''.4, 9''.4]$, $[-8''.6, 0''.0]$, $[-12''.8, 3''.5]$, and $[-14''.0, 2''.4]$. As the ACS and first-epoch NICMOS images were obtained 1.1 years apart, we can measure the field star proper motions to investigate whether any of these stars are likely companions to HD 61005. The annular proper motion of HD 61005 is $\mu_\alpha = -56.09$ mas yr^{-1} in right ascension and $\mu_\delta = 74.53$ mas yr^{-1} in declination (Perryman et al. 1997). Thus, comoving companions are expected to show a 102.61 mas displacement between the two epochs of observation.

To derive the NICMOS stellar positions, we first calculated stellar centroid positions on the image frames uncorrected for geometric distortion using the apphot center task, as described in Cox et al. (1997). We then applied a distortion correction to the raw positions using the correction coefficients appropriate for Cycle 15 data, given in the NICMOS data handbook (version 7.0). The reported rms astrometric uncertainty from applying previously derived distortion corrections to early commissioning data is 13.6 mas (Cox et al. 1997). Data obtained more recently yield similar results (e.g., Schneider et al. 2006).

The geometric distortion for the ACS data requires a low spatial frequency correction for the optical telescope assembly (OTA) and ACS optics, and two high-frequency corrections for the given wide band filter and polarizing filter (Anderson & King 2004; Kozhurina-Platais & Biretta 2004). Following Kozhurina-Platais & Biretta (2004), we first used the effective PSF library and fitting technique of Anderson & King (2000) to derive raw positions for the field stars from the flat-fielded images (*∗_flt.fits*) observed through the POL0V filter. We next applied the solution derived by Anderson & King (2004) to obtain stellar positions corrected for the low frequency OTA distortion and the high-frequency F606W filter distortion. Finally, we applied a further correction for the distortion introduced by the POL0V filter, using the solution derived by Kozhurina-Platais & Biretta (2004). The reported rms precision derived from applying this method to commissioning data is 1 mas (Kozhurina-Platais & Biretta 2004).

To test for possible companionship, we performed relative astrometry by adopting one star's position as a fixed reference point and calculating the relative proper motion for the remaining three stars. We repeated this procedure three times, using each field star as the reference. No systematic motion for any of the field stars is observed; all relative proper motions are less than twice the approximate expected rms positional accuracy ($\sigma = 13.6$ mas). We note that although the distortion solutions employed only strictly apply to noncoronagraphic, direct imaging data, the small measured astrometric offsets suggest the additional field distortions imposed by the coronagraphic optics are negligible in this case. Given that the annual proper motion of HD 61005 is significantly greater than the measured astrometric motions of all field stars, we conclude that unless all four sources are companions, the four field stars are background objects.

4. INTERPRETATION

The results presented in H07 and the previous section strongly suggest that HD 61005 is a near edge-on debris disk, undergoing significant erosion by the ambient ISM. In this section, we explore whether interaction between the disk and local interstellar gas can plausibly explain the observed swept, asymmetric morphology.

4.1. Interaction with a Cold, Dense Cloud

4.1.1. Ram Pressure Stripping of Bound Grains

In their discovery paper, H07 suggested that interaction with a cold ($T \sim 20$ K), dense ($n \sim 100$ cm^{-3}) cloud could potentially explain the HD 61005 morphology. In such a cloud, ram pressure on disk grains from interstellar gas could unbind grains from the system, analogous to the process that strips gas from cluster galaxies (Gunn & Gott 1972; van Gorkom 2004).

For ram pressure stripping to operate, the drag force on a grain must be comparable to or greater than the gravitational force binding the grain to the star. For a grain of radius $a_{\rm grain}$ and density $\rho_{\rm grain}$ orbiting at distance r from a star of mass $M_{\rm star}$,[7] the interstellar cloud density n and relative cloud-disk velocity v must obey

$$\left(\frac{n}{200\,{\rm cm^{-3}}}\right)\left(\frac{v}{30\,{\rm km\,s^{-1}}}\right)^2 \gtrsim \left(\frac{M_{\rm star}}{0.95\,M_\odot}\right)\left(\frac{a_{\rm grain}}{0.1\,\mu{\rm m}}\right) \times \left(\frac{\rho_{\rm grain}}{2\,{\rm g\,cm^{-3}}}\right)\left(\frac{70\,{\rm AU}}{r}\right)^2. \qquad (1)$$

This required density is characteristic of cold, dense gas, the existence of which is constrained in Section 4.1.3. In such a high-density cloud, H07 argued that Bondi–Hoyle–Lyttleton (BHL) accretion could also potentially play a role, leading to an accumulation of interstellar grains that contribute non-negligibly to the observed infrared excess emission and scattered light morphology.

4.1.2. *Ram Pressure Deflection of Unbound Grains*

Recently, Debes et al. (2009) suggested that ram pressure deflection of unbound grains could plausibly shape several previously resolved debris disks, including HD 61005. Their model does not specify the origin of the unbound population. However, such a substantial population of unbound grains are unlikely to be produced in a steady state situation, as collisional equilibrium models predict that the scattered light surface brightness due to bound grains dominates over that from grains unbound by radiation pressure (Krivov et al. 2006; Strubbe & Chiang 2006). Furthermore, for the case of HD 61005, radiation pressure from the low luminosity star may be insufficient to unbind grains of any size (Appendix A).

Let us nonetheless suppose that a substantial unbound grain population exists. The ambient ISM density needed to deflect such grains by the distances implied by our observations is similar to that required to strip bound grains (Section 4.1.1). Both scenarios require densities characteristic of cold, dense clouds. For $\beta = 1$ grains launched from parent bodies on circular orbits at 70 AU, the required interstellar cloud density and relative velocity obey[8]

$$\left(\frac{n}{100\,{\rm cm^{-3}}}\right)\left(\frac{v}{20\,{\rm km\,s^{-1}}}\right)^2 \gtrsim \left(\frac{M_{\rm star}}{0.95\,M_\odot}\right)\left(\frac{a_{\rm grain}}{0.1\,\mu{\rm m}}\right) \times \left(\frac{\rho_{\rm grain}}{2\,{\rm g\,cm^{-3}}}\right)\left(\frac{70\,{\rm AU}}{r}\right) \times \left(\frac{y/x}{0.2}\right)\left(\frac{110\,{\rm AU}}{x}\right). \qquad (2)$$

Here x and y, respectively, are the relative distances traveled by the grain parallel and perpendicular to the disk midplane at a given time after the grain is born. We adopt $x \sim 110$ AU and $y \sim 20$ AU, the approximate positions of the outermost binned polarization vectors in Figure 1.

4.1.3. *Limits on Cold, Dense Interstellar Gas*

The explanations of Sections 4.1.1 and 4.1.2 are hampered by two factors. First, in both circumstances, escaping grains leave the system on orbital timescales (10^2–10^3 yr). These timescales are shorter than the timescale over which the disk is expected to be collisionally replenished with submicron-sized grains ($\gtrsim 10^4$ yr; see Appendix B). Thus, both scenarios require that we are observing HD 61005 during a short-lived period in its history.

Second, cold neutral medium (CNM) clouds within the Local Bubble are extremely rare, occupying a volumetric filling factor of $\ll 1\%$ (Welsh et al. 1994). To date, only one cloud with properties typical of CNM clouds ($n \sim 50$ cm^{-3}, $T \sim 20$ K, $V = 4.9 \times 1.4 \times 0.07$ pc^3) is known within the Local Bubble ($d < 45$ pc, toward 3C 225; Heiles & Troland 2003; Meyer et al. 2006; Meyer 2007). Furthermore, in contrast to optical stellar spectra toward this known cloud, our optical spectrum of HD 61005 does not show evidence of an analogous CNM cloud. This finding is illustrated in Figure 9, which shows spectra of HD 61005 and two comparison late-type G stars (HD 33822, HD 13836) in the Na I D lines (D$_2$: 5889.95 Å; D$_1$: 5895.92 Å). HD 61005 is a relatively young star with a detected rotational velocity ($V \sin i = 9$ km s^{-1}; Holmberg et al. 2008). Thus, for direct comparison purposes, we have convolved the spectra of both HD 33822 and HD 13836 with a Gaussian of this width. In Figure 9, we have also effectively removed the stellar Doppler shift of the comparison star spectra by cross-correlating each spectrum with the HD 61005 spectrum and shifting it by the appropriate amount.

Figure 9 shows that the HD 61005 spectrum is very similar to the late-G comparison star spectra in the Na I lines. No narrow absorption component, characteristic of the known CNM Local Bubble cloud towards 3C 225, is observed (see Figure 1 in Meyer 2007). The corresponding 2σ upper limit to the Na I gas column is $\log(N_{\rm Na\,I}/{\rm cm^{-2}}) \lesssim 10.6$, based on the continuum signal-to-noise ratio (S/N ~ 100), the instrumental resolution ($R \sim 60{,}000$), a linewidth characteristic of the nearby cold cloud toward 3C 225 ($b = 0.54$ km s^{-1}), and assuming the linear regime of the curve of growth. This upper limit translates into a total hydrogen column of $\log(N_{\rm H\,I+H_2}/{\rm cm^{-2}}) \lesssim 19.0$, employing the sodium–hydrogen conversion relation derived by Ferlet et al. (1985). The scatter in this relation is such that a third of measured hydrogen columns deviate from their predicted columns by factors of a few (Wakker & Mathis 2000). Taking this into account, our predicted hydrogen upper limit is still well below the columns expected for CNM clouds (10^{20}–10^{21} cm^{-2}; McKee & Ostriker 1977) and also below the mean column density of Na I detected toward 3C 225: $\langle\log(N_{\rm Na\,I}/{\rm cm^{-2}})\rangle = 11.7$ (Meyer et al. 2006).

There are a few examples of tiny ($\lesssim 1000$ AU) low column density ($\log(N_{\rm H\,I+H_2}/{\rm cm^{-2}}) \lesssim 19.0$) cold clouds in the literature (e.g., Heiles 1997; Stanimirović & Heiles 2005). These clouds constitute $\lesssim 2\%$–4% of the total neutral hydrogen column along the lines of sight in which they are detected. The precise frequency of these clouds is not well constrained by large-scale surveys, as their low columns are similar to survey detection thresholds ($\sim 10^{18}$ cm^{-2}; Heiles & Troland 2003). However, an upper limit to their frequency can be obtained by noting that $\gtrsim 5$ such clouds along a typical line of sight would lead to their

---

[7] Throughout this paper, we adopt $M_{\rm star} = 0.95\,M_\odot$, based on the pre-main-sequence evolutionary tracks of D'Antona & Mazzitelli (1997) and Baraffe et al. (1998) and the FEPS age estimate reported by H07 (E. Mamejek 2009, private communication).

[8] Note that Equations (1) and (2) assume the cross-section grains present to interstellar gas equals the geometric cross section; calculations performed using ballistic cluster–cluster aggregates and ballistic particle–cluster aggregates suggest this assumption is good to within an order of magnitude (Minato et al. 2006).

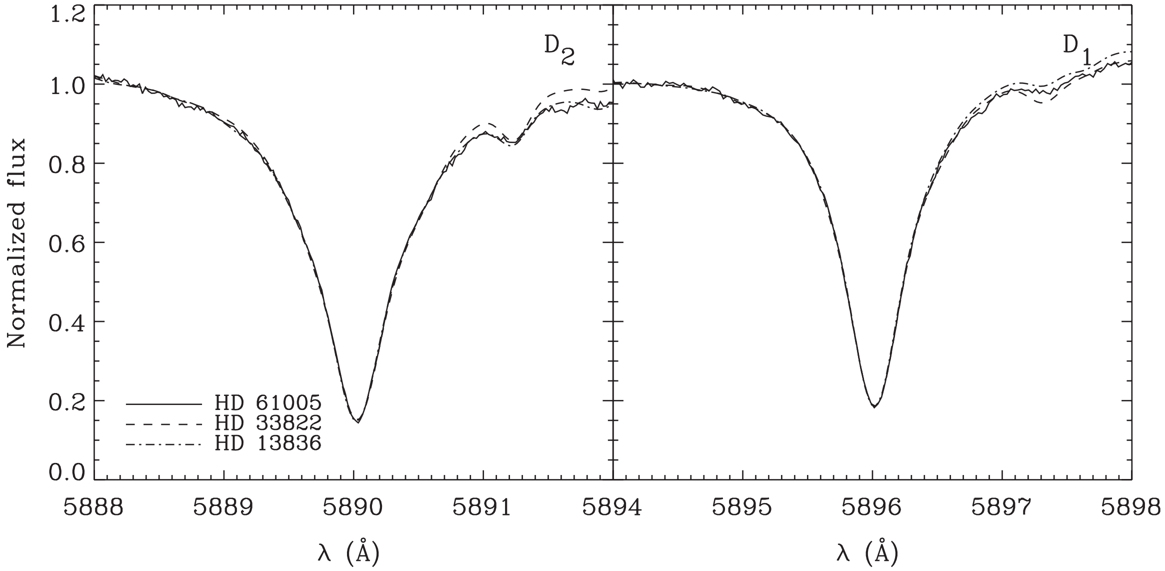

Figure 9. Optical spectrum of HD 61005 and two comparison late-type G-star spectra in the Na I D lines. The Na I lines in HD 61005 are very similar to the comparison star lines. No narrow absorption component expected for an intervening dense cold interstellar cloud is observed, placing limits on the potential effectiveness of ram pressure stripping of bound grains and deflection of unbound grains in the HD 61005 system.

systematic detection in large-scale surveys (C. Heiles 2009, private communication). Thus, within the Local Bubble ($d \lesssim 100$ pc), these tiny, dense clouds occupy $\lesssim$0.025% of the distance along a typical line of sight. At present, only two dozen debris disks have been spatially resolved. Therefore it seems unlikely that we have already imaged a debris disk residing in one of these clouds. Interaction with a cold, dense cloud is thus an unsatisfactory explanation for the swept morphology observed in HD 61005.

4.2. Interaction with a Warm, Low-density Cloud

Given that disk interaction with a cold, dense cloud appears unlikely, we explore in this section whether interaction with a warm, low-density cloud can potentially explain the observed morphology.

4.2.1. Ram Pressure Stripping of Disk Gas and Entrainment of Disk Grains

Warm ($T \sim 7000$ K) interstellar clouds dominate the mass of the local ISM (e.g., Frisch 2004) and occupy a local volume filling factor of ~5.5%–19% (Redfield & Linsky 2008). Our optical spectrum does not constrain the presence of such a cloud toward HD 61005, as typical columns towards these clouds are $N_{\rm H\,I} \sim 10^{17}$ cm^{-2} (Redfield 2006).

The low densities of warm local clouds are insufficient to supply a ram pressure force comparable to the gravitational force and thereby directly unbind grains from the system. For typical parameters of warm local interstellar clouds ($n_{\rm H\,I} = 0.2$ cm^{-3}, $v_{\rm rel} = 25$ km s^{-1}; Redfield 2006) and 0.1 μm disk grains, the ram pressure stripping radius is ~10^3 AU (Equation (1)), much larger than the radius of the observed bow structure (~2″ = 69 AU).

However, in principle, ram pressure stripping could still play a role if the HD 61005 disk contains gas that is undergoing ram pressure stripping by the ISM. In this scenario—in contradistinction to the direct ram pressure stripping scenario outlined in Section 4.1.1—disk grains are swept away by the interstellar flow only because they are entrained in outflowing disk gas. Gas–gas interactions correctly explain the H I morphologies of galaxies traveling through an intracluster medium (van Gorkom 2004); the truncated, swept-back H I disks of galaxies strongly resemble HD 61005 (e.g., see Figures 1.7 and 1.8 of van Gorkom 2004). We show below, however, that this interpretation for HD 61005 is incorrect because the requirement on the density of disk gas is incompatible with the requirement that grains be entrained.

To unbind disk gas, the ISM ram pressure must exceed the gravitational force per unit disk area:

$$n\mu v^2 \gtrsim GM_{\rm star}\sigma/r^2, \tag{3}$$

where $\mu \approx 2 \times 10^{-24}$ g is the mean molecular weight of the ISM and σ is the surface mass density of disk gas. For parameters appropriate to a warm cloud (Redfield 2006), all disk gas having a surface density

$$\sigma \lesssim 4 \times 10^{-8} \left(\frac{r}{100\ \rm AU}\right)^2 \left(\frac{0.95\ M_\odot}{M_{\rm star}}\right) \left(\frac{n}{0.2\ \rm cm^{-3}}\right) \times \left(\frac{v}{25\ \rm km\ s^{-1}}\right)^2\ \rm g\ cm^{-2} \tag{4}$$

is swept away by the ISM. The circumstellar gas content of HD 61005 is unknown.

For unbound disk gas to entrain disk grains, the momentum stopping time of a grain in gas cannot be much longer than the outflow timescale, $1/\Omega$, over which marginally unbound gas departs the system, where Ω is the Kepler orbital frequency. From Weidenschilling (1977), the momentum stopping time of a grain in rarefied gas is given by the Epstein (free molecular drag) law as

$$t_{\rm stop} \sim \frac{1}{\Omega}\frac{a_{\rm grain}\rho_{\rm grain}}{\sigma} \sim \frac{500}{\Omega}\left(\frac{a_{\rm grain}}{0.1\ \mu\rm m}\right)\left(\frac{\rho_{\rm grain}}{2\ \rm g\ cm^{-3}}\right) \times \left(\frac{4\times10^{-8}\ \rm g\ cm^{-2}}{\sigma}\right), \tag{5}$$

which is too long compared to the outflow time. Thus, we discount the possibility that the observed disk morphology arises from ram pressure stripping of disk gas.

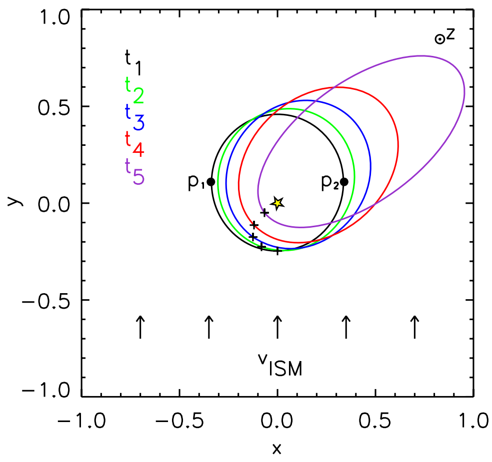

Figure 10. Orbital evolution of a test particle in the x–y plane under the effect of neutral gas drag. Five time periods separated by a fixed number of orbits are shown. The grain begins with its star–pericenter (Runge–Lenz) vector anti-aligned with the incoming interstellar flow, directed along the positive y-axis, and its angular momentum vector aligned with the z-axis (out of the page). The ISM flow decelerates the grain on one leg (e.g., point p_1) and accelerates it on the other (e.g., point p_2), causing the Runge–Lenz vector to rotate. The grain's periastra at each successive time is shown by a cross to illustrate this effect.

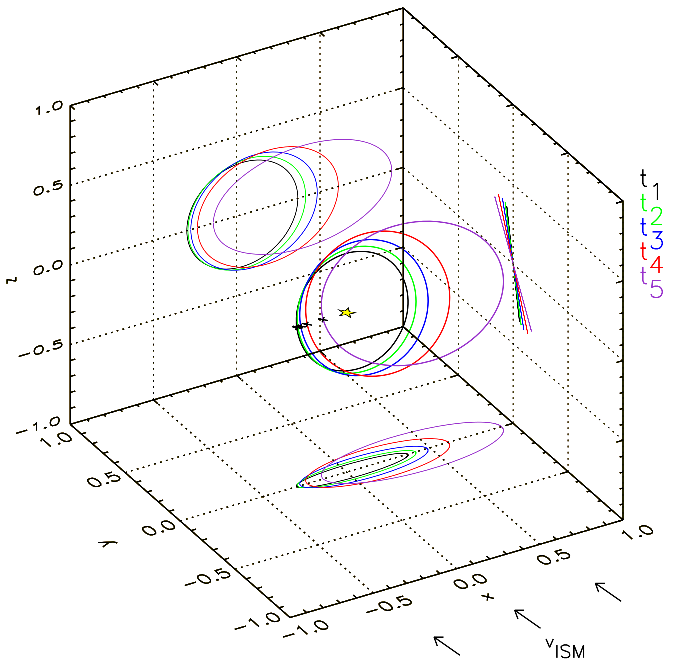

Figure 11. Orbital evolution due to neutral gas drag of a test particle initially inclined by 80° with respect to the incoming flow. Five time periods separated by a fixed number of orbits are shown. The grain's initial Runge–Lenz vector is chosen to be at its equilibrium orientation. The ISM flow exerts a net torque on the orbiting grain, causing the angular momentum vector to rotate into a direction perpendicular to the ISM flow.

4.2.2. *Secular Perturbations to Grain Orbits Induced by Ram Pressure*

The direct ram pressure stripping scenario described in Section 4.1.1 requires that the ISM ram pressure force on disk grains be comparable to the stellar gravitational force. As shown in Section 4.2.1, this condition is not met in low-density warm clouds, for which $F_{\rm ram}/F_{\rm grav} \sim 10^{-3}$ (at ∼70 AU; see Equation 1). However, even in the case when the force exerted by interstellar gas is much less than the gravitational force, neutral gas can introduce secular perturbations to bound grain orbits that could significantly change the morphology of the disk over timescales of $\sim 10^3$–10^4 yr, assuming submicron-sized grains dominate the scattered-light distribution. This perturbation timescale is less than the crossing time of local warm clouds: $t_{\rm cross} \sim (L_{\rm cloud}\,/\,5~{\rm pc})/(v_{\rm rel}\,/\,25~{\rm km~s^{-1}}) \sim 10^5$ yr (Redfield 2006). Thus, this mechanism can plausibly explain the disturbed HD 61005 morphology. Interestingly, this scenario has been proposed as the primary removal mechanism for dust in our own solar system at 20–100 AU (Scherer 2000), though at present, little empirical evidence is available to test this theory.

As described in Scherer (2000), the underlying physical process responsible for neutral gas drag is similar to that responsible for solar wind drag. In both cases, momentum transfer from incident protons or gas particles to the grain surface results in secular perturbations to the grain's initial orbit. However, the monodirectional character of the interstellar gas drag force leads to changes in particle orbits that are very different from those induced by the solar wind. While the solar wind and Poynting–Robertson drag both act to reduce grain eccentricities and semi-major axes, interstellar gas drag tends to increase them, eventually unbinding the grains from the system.

In the absence of other perturbing forces, the analytic work of Scherer (2000) shows that the gas drag force acts to rotate a given particle's orbital plane into a plane coplanar to the flow vector, and its star–pericenter (Runge–Lenz) vector into a direction perpendicular to the flow vector. These effects are illustrated in Figures 10 and 11, which show the orbital evolution of two dust grains with different initial orbital elements. The grain in Figure 10 starts on a low-eccentricity ($e = 0.3$) orbit in the x–y plane with its Runge–Lenz vector anti-aligned with the incoming interstellar flow and its angular momentum vector aligned with the z-axis (out of the page). This orientation causes the grain to be decelerated on one leg (e.g., point p_1) and accelerated on the other (e.g., point p_2), causing the Runge–Lenz vector to rotate. The grain's periastron at each successive time is denoted by a cross to highlight this effect. The rotation continues until the Runge–Lenz vector becomes perpendicular to the incoming flow. Thus, counterintuitively, neutral gas drag leads to a buildup of grains perpendicular to the relative flow direction.

The tendency of neutral gas drag to rotate a given grain's orbital plane into a direction coplanar with the incoming flow is illustrated in Figure 11, which shows the evolution of a low-eccentricity ($e = 0.1$) grain initially inclined 80° with respect to the ISM flow. The grain's initial Runge–Lenz vector is chosen to be at its equilibrium orientation (perpendicular to the flow) to isolate the effect of the orbital plane rotation. The ISM flow exerts a net torque on the orbiting grain, causing the angular momentum vector to rotate into a direction perpendicular to the incoming flow. This effect is easiest to discern from the two-dimensional projection of the y–z plane in Figure 11.

The above discussion suggests that rigorously modeling the neutral gas drag effect requires knowledge of the initial grain orbital elements and the interstellar gas flow. However, for the case of HD 61005, neither of these prerequisites is known. HD 61005 has a well-determined space motion; the *Hipparcos*-measured proper motion corresponds to a plane-of-sky velocity of $v_\alpha = 9.2 \pm 0.3~{\rm km~s^{-1}}$, $v_\delta = 12.2 \pm 0.4~{\rm km~s^{-1}}$ at the distance of HD 61005. The radial velocity is $v_r = 22.3 \pm 0.2~{\rm km~s^{-1}}$ (Nordström et al. 2004). However, the velocity of the putative cloud responsible for the swept morphology is unknown. Velocities of local warm clouds can be comparable to the observed space motion of HD 61005 (Frisch et al. 2002). Thus, the red arrow in Figure 3 of H07 denoting the direction of the star's tangential motion is not a reliable indicator of the cloud–star relative velocity.

Unfortunately, HD 61005 is difficult to assign to any known interstellar clouds, owing to its heliocentric distance (34.5 pc) and galactic coordinates ($l = 246\fdg4$, $b = -5\fdg6$). Redfield & Linsky (2008) recently used radial velocity measurements of 157 lines of sight to identify 15 warm clouds in the local ISM. However, the identified clouds are thought to reside largely within 15 pc of the Sun, whereas the distance to HD 61005 is 34.5 pc. Furthermore, the line of sight to HD 61005 is not assigned to any of these clouds. The star's galactic coordinates could plausibly associate it with either the G cloud or the Blue cloud (e.g., see Figure 19 in Redfield & Linsky 2008), though HD 61005 is more likely associated with a more distant, currently unidentified cloud, rendering the cloud–star relative velocity for this system highly uncertain.

The initial orbital elements prior to the presumed cloud interaction are similarly unknown. The radial architectures of debris disks in scattered light show significant diversity and currently appear largely independent of other observables, such as age or spectral type (Kalas et al. 2006). Furthermore, as discussed in Section 3.1.4, the one-dimensional surface brightness profiles of HD 61005 do not allow us to place strong constraints on the location of the parent body population, and thus the grain eccentricities and inclinations. We do note, however, that the submicron particle sizes implied by the polarization and color measurements do not a priori contradict the bound orbits requirement of the gas drag perturbation theory, as radiation pressure from the star is likely insufficient to unbind grains of any size (Appendix A).

Given the large uncertainties in the disk and ambient ISM properties of the HD 61005 system, we are unable to empirically test whether gas drag is responsible for the asymmetric, swept morphology. Therefore, to explore whether this mechanism can plausibly explain the observed structure, we adopt the numerical techniques described in Scherer (2000) to construct a modest grid of models with reasonable assumptions for the disk grains and ISM. Details of the model construction and restrictions are described in Appendix B. In summary, we subject a ring of 0.1 μm, low eccentricity ($e = 0.2$) grains with semi-major axes of 60 AU and random inclinations to a uniform density cloud typical of nearby warm interstellar clouds ($n_{\rm H\,I} = 0.2$ cm^{-3}) traveling at a typical cloud–star relative velocity of $v_{\rm rel} = 25$ km s^{-1} (Redfield 2006). We test a range of relative flow vectors and produce scattered light images from the resultant grain distributions after the system has achieved a steady state.

The resulting grid of models produced for a range of relative flow directions and disk inclinations is presented in Figures 12–14. Each frame is 9″ across, and the color scale is logarithmic. The adopted coordinate system is described in Appendix B. A comparison of Figure 1 to Figures 12–14 suggests that none of the IS gas drag models are a striking match to the data. On the other hand, a gross swept morphology, somewhat similar to HD 61005, is present in a few of the model panels. These best approximations correspond to disk inclinations of $i = \pm 80^\circ$, consistent with the data (Section 3.1.2), and relative flow directions largely coplanar with the disk midplane, approximately in the plane of the sky (Figure 12, panels $\theta \sim 0^\circ$, 180°). This relative flow direction is counterintuitive, going against the flow direction suggested by preliminary inspection of the scattered-light images, perhaps providing a further strike the against IS gas drag interpretation. On the other hand, if these preliminary models are a first approximation of the data, then this distinctive relative velocity may be verified by future observations (Section 5.1).

For ease of viewing, we show in Figure 15 the ACS and NICMOS data together with a neutral gas drag model that roughly approximates the observed morphology, corresponding to the top row, third panel of Figure 12. A summary of the morphological shortcomings of this strongest IS gas drag model can be summarized as follows.

1. The swept back components NE2 and SW2 are much more extended relative to the main disk in the data than in the model.
2. The edges of the swept back structure are more pronounced in the data than in the model.
3. The sharp radial spurs observed beyond the inflection point along components NE1 and SW1 are not present in the model.
4. The model figure does not show the significant brightness asymmetry between the northeast and southwest disk lobes that is seen in the data.

These differences could indicate that the physics incorporated into the current IS gas drag models is overly simplistic (Section 5.1), or that interstellar gas drag is not responsible for the observed morphology (e.g., Section 5.3).

As discussed in Section 3.1, the ACS polarization results can be understood qualitatively through geometric considerations alone. Thus, the most promising IS gas drag models naturally reproduce the observed polarization structure.

5. DISCUSSION

5.1. Interstellar Gas and the HD 61005 Morphology

The previous section explored whether disk/gas interaction can plausibly explain the unusual HD 61005 morphology. Of the four scenarios considered, three are implausible, given the limits on the ambient interstellar gas density imposed by our optical spectrum. The fourth scenario, secular perturbations from low density gas, is an attractive alternative, as this mechanism can significantly distort grain orbits well within a cloud crossing time. Furthermore, the densities required by this scenario are typical of local interstellar clouds, which occupy up to ∼20% of the local ISM.

Nevertheless, our preliminary modeling of this effect (Figures 12–14) can only produce disk morphologies in very rough agreement with the observations, suggesting that either additional physics needs to be incorporated into the current models, or that an altogether distinct physical mechanism is at work. Indeed, the current models are simplistic, and their applicability is limited by several key assumptions.

1. *Astrosphere sizes.* As discussed by Scherer (2000), the toy models presented in Figures 12–14 require that the disturbed grains be inside the astrospheric termination shock, such that the interstellar gas density and velocity can be approximated as constant. For the case of HD 61005, the termination shock distance is unknown. Furthermore, as HD 61005 is farther away than any star for which a direct astrospheric detection has been made (Wood 2004), the astrosphere size may be difficult to constrain observationally. In general, termination shock distances vary greatly, depending on the ambient ISM and stellar wind conditions (e.g., densities, temperatures, velocities, stellar

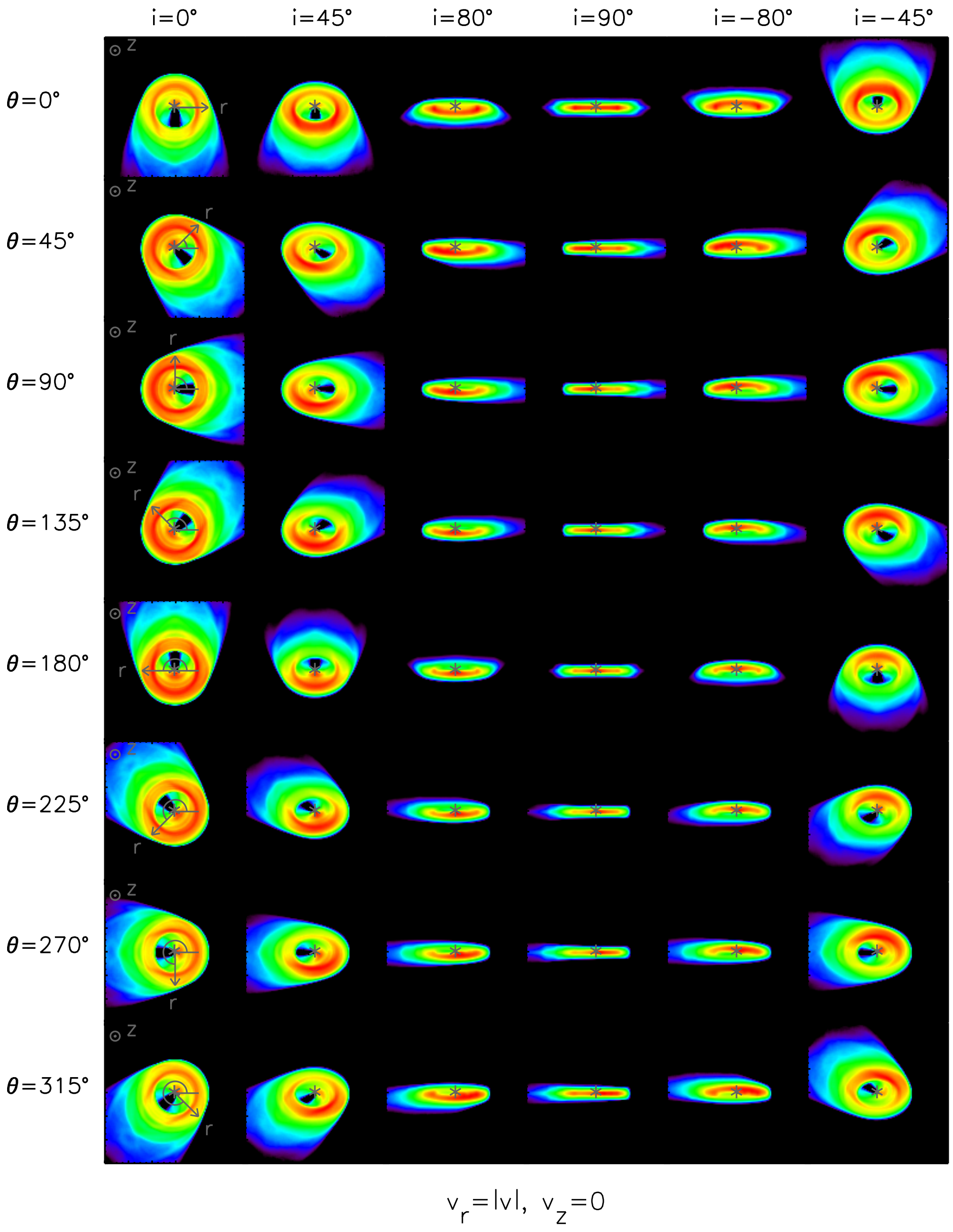

Figure 12. Steady state model images for hypothetical debris disk systems undergoing neutral gas perturbations. In all models, the relative flow is coplanar with the disk midplane. The adopted cylindrical coordinate system is shown with respect to the face-on disks in the left column. The vector $\boldsymbol{r}$ points in the direction of the relative ISM flow; the azimuthal orientation of $\boldsymbol{r}$ is defined by θ. The disk inclinations are indicated at top. Each box is $9'' \times 9''$ (assuming a distance to the system of 34.5 pc); the color scale is logarithmic. The models show that brightness asymmetries, bow structures, and swept morphologies can all be produced by disk encounters with warm interstellar clouds, which occupy a sizable fraction of the local ISM.

activity). For the case of the Sun only, the hydrodynamic models of Müller et al. (2006) show that the termination shock distance could easily vary between ∼10 AU and 500 AU. Observational astrosphere measurements of solar-type stars are consistent with these predictions[9] (Mann et al. 2006, and references therein).

2. *Initial conditions.* As noted in Section 4.2.2 and Appendix B, our adopted initial orbital elements for the HD 61005 disk grains prior to the interstellar cloud interaction are highly uncertain, given a lack of information for the grain properties and underlying planetesimal population that collisionally replenishes the observed dust disk. Future long-wavelength observations sensitive to larger grains may be able to place tighter constraints on the distribution of submicron grains prior to the interstellar cloud interaction, as the distribution of large grains would likely reflect that of the parent bodies for the submicron population. Furthermore, larger grains would not be significantly affected by interstellar gas drag on the same timescale as the submicron size grains traced in these observations. The numerical techniques employed here and in Scherer (2000) can be easily revised to accommodate an arbitrary initial disk architecture, provided the orbits are not highly eccentric, such that

---

[9] On a broader scale, no astrosphere detections have been made for stars earlier than G-type. As a result, the typical effect of astrospheres on IS gas drag in debris disks surrounding A-type stars is difficult to reliably assess.

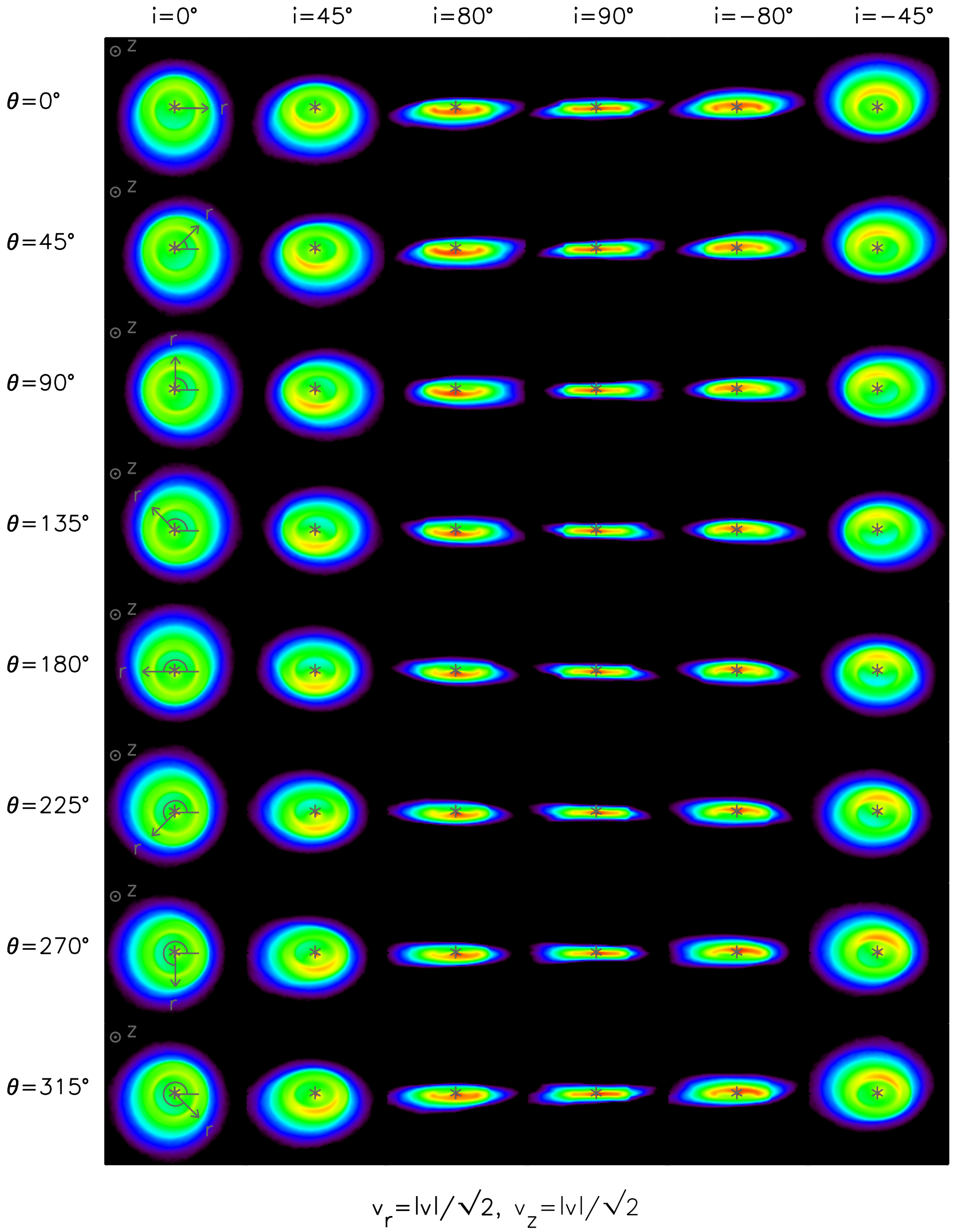

Figure 13. Same as Figure 12, only with components of the relative flow both coplanar with the disk midplane and perpendicular to it. The radial and perpendicular flow components are equal in magnitude.

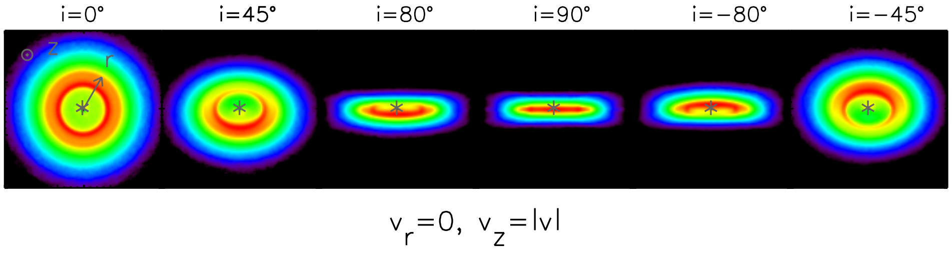

Figure 14. Same as Figures 12 and 13, only with the relative flow vector oriented purely perpendicular to the disk midplane. The dust distribution in these models is largely axisymmetric, as described in the text. The brightness asymmetries evident at intermediate inclinations ($i = 45°, 80°, -80°, -45°$) are the result of scattering asymmetry; for positive inclinations, the lower half of the disk in the image is closer to the observer than the upper half.

averaging over one orbit and applying Gauss' method is invalid.

3. *Internal disk collisions.* In Appendix B, we estimate to order-of-magnitude that the collision time for submicron grains at ~70 AU is ~5000 yr. This collision time is somewhat longer than the timescale over which our model relaxes to a steady state—essentially the time for gas drag to unbind a grain—given in Appendix B as ~3000 yr. That the times are comparable supports the assumption of our models that each grain removed by gas drag is collisionally replenished. At the same time, the comparison of timescales underscores a shortcoming of our model—that removal of

grains by collisions is ignored. In reality, submicron grains should be removed from the system not only by gas drag, but also by collisions, in roughly equal proportions. We defer to future work a comprehensive study that includes removal by collisions via a collisional cascade.

4. *Planetary configurations.* Finally, as illustrated by Scherer (2000, e.g., his Figure 2), the incorporation of planetary orbits can appreciably change the perturbed orbital elements from the case in which only IS gas drag is considered. This caveat is especially important for massive grains, or grains in close proximity to planetary orbits. As a result, the models presented here should be treated with some caution if applied to typical planetary system scales ($\lesssim$50 AU; e.g., Kenyon & Bromley 2004). This cautionary point may be particularly important for the case of HD 61005, as the origin of the brightness asymmetry between the northeast and southwest disk lobes (Section 3.1.1) is unknown. The agreement between the northeast and southwest deflected component P.A. (Section 3.1.3 and Figures 1–2) suggests that this asymmetry may originate from a physical mechanism entirely distinct from ISM interaction. If the asymmetry is due to a massive perturber, the disk morphologies produced in Figures 12–14 are likely to be inapplicable. Resolved long wavelength observations sensitive to massive grains are needed to further explore this possibility.

In addition to the above uncertainties, a remaining ambiguity important for future IS gas drag modeling is the velocity of the putative cloud responsible for the HD 61005 morphology. H07 noted that the star's tangential space motion is perpendicular to the disk midplane, in agreement with the relative flow vector suggested by initial inspection of the observed images. However, while assigning the relative flow direction to the star's tangential velocity is appealing, the three scenarios explored in Section 4 which assume this flow direction were found to be untenable. Furthermore, velocities of local warm clouds can be comparable to the observed space motion of HD 61005 (Section 4.2.2). As a result, the star's tangential motion is not a reliable indicator of the cloud–star relative velocity.

Future spectroscopic observations may be able to detect the cloud directly (e.g., *HST*/GO Program 11674; PI: H. Maness), thereby providing key constraints on the ambient ISM density and velocity. Such observations will greatly inform future modeling, as the preliminary interstellar gas drag models presented here suggest a counterintuitive relative motion parallel to the disk midplane, rather than perpendicular to it. Though HD 61005 is difficult to assign to any known interstellar clouds (Section 4.2.2), its galactic coordinates could plausibly associate it with either the G cloud or the Blue cloud. The space velocities of both of these clouds suggest a relative motion dominated by the radial velocity component. Therefore, if HD 61005 is associated with either of these clouds, the relative motion is inconsistent with all models posited in Section 4.

5.2. *General Applicability of Interstellar Gas Drag*

The normalcy of the interstellar densities, velocities, and cloud sizes required by the secular perturbation model in Section 4.2.2 suggests that IS gas drag can be important beyond HD 61005 in shaping debris disk morphologies. Taking the simple models of Section 4.2.2 and Appendix B at face value, several of the general morphological features produced in Figures 12–14 are consistent with observed disk structures. For example, the extreme brightness asymmetry in HD 15115 (Kalas et al. 2007) may potentially result from interstellar gas drag, though a range of alternative explanations could explain this system as well (e.g., see list in Section 1). The bow structures seen in some of the face-on models in Figure 12 are also reminiscent of the mid-infrared morphology observed around the A star, δ Velorum, which was recently modeled as a purely interstellar dust phenomenon (Gáspár et al. 2008). Finally, the middle panels in Figure 13 show that warps, similar to that seen in β Pic (e.g., Mouillet et al. 1997), can in principle be produced for a relatively wide range of flow directions.

However, while IS gas drag can in principle produce commonly observed disk features, the rate at which gas drag is expected to affect the observations remains unclear. Beyond the uncertainties in the model physics described in Section 5.1, the characteristics of warm, low density clouds are currently uncertain, as detailed knowledge of them is limited to clouds residing predominantly within 15 pc of the Sun (Redfield & Linsky 2008). As a result, our understanding of typical cloud sizes, shapes, and total volumetric filling factor remains rudimentary. A key finding in this area, however, is that a significant fraction of nearby warm clouds appear to exhibit filamentary morphologies, which would limit the average interaction time between a given disk and cloud, likely reducing the rate at which IS gas perturbations produce an observable effect. This concern is particularly important for the case of disks surrounding early-type stars, as grains traced in scattered light tend to be larger in disks surrounding A-type stars than in their later type counterparts, owing to the larger radiation pressure blowout size. As such, the scattered-light morphologies for A-star disks require correspondingly longer cloud–disk interaction times to be noticeably affected. The timescale for a given grain to become unbound under IS gas drag increases approximately as the square root of the grain size (Scherer 2000).

5.3. *Interstellar Grains and the HD 61005 Morphology*

Finally, we note that all models posited in Section 4 consider only the role of interstellar gas, ignoring the potential effects of interstellar grains. Artymowicz & Clampin (1997) investigated IS sandblasting of debris disks surrounding A stars and found that sandblasting has a negligible effect on the observed structure, as radiation pressure blows out most incoming interstellar grains before they are allowed to intersect the disk. However, under this framework, only grains with $\beta \geqslant 1$ are ejected. Thus, Figure 16 shows that radiation pressure does not protect the HD 61005 disk, as it does in A-stars.

Nevertheless, even if radiation pressure does not protect the disk against sandblasting, the stellar wind might, as only large interstellar grains with sizes greater than a few $\times 0.1$ μm are allowed to enter astrospheres freely without deflection (Linde & Gombosi 2000). Thus, it is likely that interstellar sandblasting can only plausibly compete with interstellar gas drag if the astrosphere is smaller than or comparable to the observed debris disk size (Mann et al. 2006). The size of the HD 61005 astrosphere is unconstrained by present observations. In general, observations and models of astrospheres surrounding solar-type stars show sizes in the range $\sim$10–10^3 AU, depending on the ambient ISM and stellar wind conditions (see discussion in Section 5.1). Thus, with a characteristic disk size of $\lesssim$70 AU, it is not clear whether typical interstellar grains can intersect the HD 61005 disk.

Detailed modeling of sandblasting is outside the scope of this paper. However, future theoretical work should investigate the effects of sandblasting on debris disks surrounding solar-type

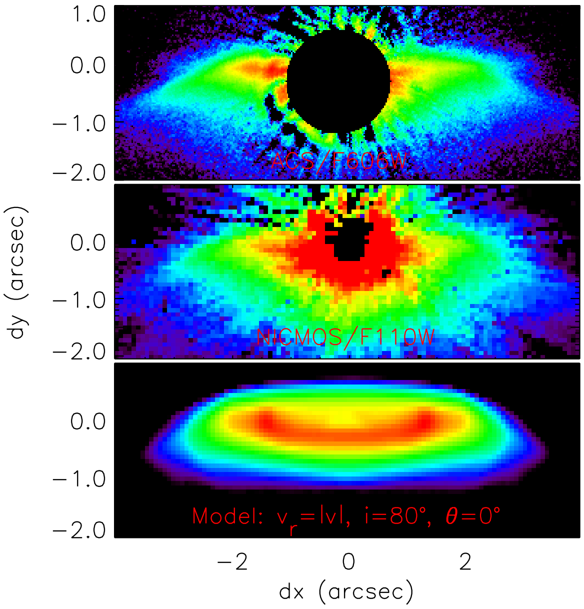

Figure 15. Comparison between the ACS Stokes *I* image (top), the NICMOS 1.1 μm image (middle), and a promising neutral gas model (bottom), taken from Figure 12 (top row, third column). This comparison shows that the simple model presented here is only a very rough representation of the data. Still, the gross swept, asymmetric morphology is clearly present in the model image.

stars. Calculations of the ISM density required for sandblasting to eject an observable flux of grains, the disk morphologies produced in this case, and the timescale for which sandblasting can be sustained would significantly aid in differentiating between this explanation and the gas drag models presented here.

6. SUMMARY

The morphology and polarization structure of HD 61005 in the *HST*/ACS data (Figures 1–3) strongly suggest that HD 61005 is a debris disk undergoing significant erosion by the ambient ISM. The physical mechanism responsible for this erosion remains uncertain. Previous work has suggested that HD 61005 may be interacting with an unusually dense cloud. However, our high-resolution optical spectrum argues against this idea, instead suggesting an ambient ISM density typical of local interstellar clouds. Thus, the evolutionary state of HD 61005 may represent a commonplace, intermittent stage of debris disk evolution driven by interaction with typical, low-density gas.

With this motivation, we considered the effects of secular perturbations to grain orbits induced by ram pressure in warm, tenuous clouds. This mechanism can significantly distort grain orbits within a typical cloud crossing time and generate structures that very roughly reproduce the HD 61005 images. Future work that incorporates additional, more detailed physics may improve the agreement between the observations and interstellar gas drag models. The theoretical effects of interstellar sandblasting for solar-type stars should also be investigated in greater detail.

Regardless of the interpretation for HD 61005, we expect interstellar gas drag is important at some level in shaping the structure and evolution of planetary debris disks. The frequency with which this effect is important strongly depends on the typical sizes, shapes, velocities, and filling factors of warm interstellar clouds, which have poorly constrained global properties at present. Nevertheless, some morphological features common to nearby resolved debris disks (e.g., brightness asymmetries, warps, and bow structures) can in principle be produced in this way. A larger sample of spatially resolved debris disks at a wide range of wavelengths and more detailed theoretical work will help eliminate some of these remaining ambiguities.

We wish to thank Jay Anderson and Vera Platais for providing the astrometric software used to test for companionship. We also thank Carl Heiles, Gaspard Duchene, Seth Redfield, and Marshall Perrin for useful conversations that helped shape the ideas discussed in this paper. H.M. is funded by the GRFP at NSF and the GOPF at UC Berkeley. Support for this work was provided by NASA through grant number GO-10847

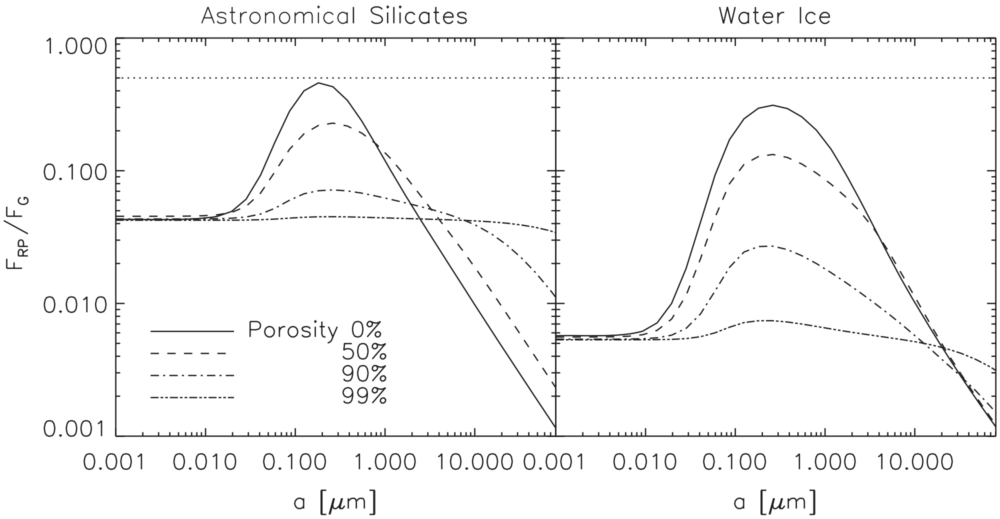

Figure 16. Ratio of the radiation pressure force to gravity (β) for astrophysical silicate grains (left) and water ice (right) for the HD 61005 system. The horizontal dotted line indicates the ratio above which grains launched by parent bodies on circular orbits become unbound. Thus silicate and ice grains in a conventional debris disk surrounding a solar type star are likely to remain bound to the star. On the other hand, the weak radiation field ($\beta < 1$) implies that radiation pressure alone does not impede interstellar grains from entering the system. Thus if the astrosphere surrounding HD 61005 is smaller than the disk, interstellar sandblasting could potentially erode the HD 61005 disk grains.

from the Space Telescope Science Institute, which is operated by Association of Universities for Research in Astronomy Incorporated, under NASA contract NAS5-26555. This work was also supported in part by the University of California Lab Research Program 09-LR-01-118057-GRAJ and NSF AST-0909188.

APPENDIX A

RADIATION PRESSURE AND BLOW-OUT

To provide a preliminary assessment of the unbound grain contribution, we compute the radiation pressure force according to Kruegel (2003)[10]:

$$F_{\rm RP} = \int \frac{\pi a^2}{c} (1 - g_\nu \omega_\nu) Q_\nu^{\rm ext} F_\nu \, d\nu. \quad \text{(A1)}$$

Here, g_ν is the grain scattering asymmetry, ω_ν is the albedo, and $Q_\nu^{\rm ext}$ is extinction cross section in units of the geometric cross section. H07 and Carpenter et al. (2008) showed that the stellar spectral energy distribution of HD 61005 is well-matched by a main-sequence $T_{\rm eff} = 5456$ K Kurucz model atmosphere. We therefore use their best-fit spectrum in evaluating Equation (A1) to interpolate between the data and to extrapolate for the small fraction of missing flux longward of 24 μm and shortward of 0.3 μm.

Figure 16 shows the ratio of the radiation pressure to gravitational force, $\beta = F_{\rm RP}/F_{\rm G}$, for spherical particles with scattering properties computed using Mie theory. Results are shown for water ice ($\rho = 1$ g cm^{-3}; Warren 1984) and Draine's astrophysical silicate ($\rho = 3.5$ g cm^{-3}; Draine & Lee 1984). Mie theory radiation pressure calculations for silicate grains have been verified to within factors of a few using results from microwave analog laboratory data, computational discrete dipole approximation (DDA) and *T*-matrix calculations, and solar-system collection experiments (Wehry et al. 2004; Landgraf et al. 1999, and references therein). Solar-system calculations performed on non-spherical, ballistic particle–cluster aggregates and ballistic cluster–cluster aggregates also yield similar results to spherical-grain Mie theory calculations (e.g., Figure 7 Mann et al. 2006, and references therein). For the various porosities shown in Figure 16, we used the Maxwell–Garnett rule to compute the approximate dielectric constant for a dilute medium. As applied to debris disk systems, this method has been found to agree well with DDA calculations for aggregate porosities of $P \lesssim 90\%$ (Köhler & Mann 2004).

The calculation in Figure 16 does not include the effect of stellar wind pressure, as the stellar wind parameters for HD 61005 are unknown, and the X-ray flux of HD 61005 ($F_X = 4 \times 10^6$; Wichmann et al. 2003) exceeds the maximum value for which the F_X–$\dot{M}_*$ relation of Wood et al. (2005) is reliable. Nevertheless, evaluating Equation (7) from Strubbe & Chiang (2006) in the geometric optics limit, stellar wind pressure is predicted to be over an order of magnitude less significant than radiation pressure, even for mass loss rates approaching $\dot{M}_* \sim 100\, \dot{M}_\odot$, approximately the highest mass loss rate yet observed. Thus, the radiation pressure force of Figure 16 is expected to be representative of the total outward pressure force, independent of the stellar mass loss rate.

If a grain is liberated from a parent body that is on a circular orbit, radiation pressure increases its eccentricity such that $e = \beta/(1-\beta)$; for $\beta \geqslant 1/2$, the grain is launched onto an unbound orbit. Debris disk grains tend to be highly porous with vacuum volume filling fractions of ~90% (e.g., Li & Greenberg 1998; Graham et al. 2007). Thus, Figure 16 shows that silicate and ice grains in a conventional debris disk surrounding a late-G star like HD 61005 are likely to remain bound to the star, unless the parent body population is highly eccentric.

APPENDIX B

NEUTRAL GAS DRAG TOY MODELS

B.1. *Model Construction and Results*

The time for a 0.1 μm grain to become unbound by interstellar gas drag is $\sim 10^3$–10^4 years, depending on the ambient ISM density, velocity, and relative flow direction, and the initial orbital elements of the grain (more precise estimates are given later in this section). This timescale may be compared to the collision time for submicron grains. Low eccentricity (e = 0.1–0.2) grains are pumped to moderate eccentricities (e = 0.3–0.4) by interstellar gas drag within a typical orbital period of 500 yr. Thus, combining Equations (7) and (9) from Chiang et al. (2009) for moderately eccentric grains, the approximate collisional lifetime of submicron sized grains is

$$t_{\rm col} \sim 5000\,{\rm yr}\, \frac{2\times10^{-3}}{L_{\rm IR}/L_*} \frac{H/R}{0.1} \sqrt{\frac{\Delta R/R}{0.2}} \left(\frac{0.95\,M_\odot}{M_*}\right)^{1/2} \times \left(\frac{R}{70\,{\rm AU}}\right)^{3/2} \left(\frac{1-0.4}{1-e}\right)^{3/2}. \quad \text{(B1)}$$

Here, the fractional luminosity, $L_{\rm IR}/L_* = 2 \times 10^{-3}$, is taken from H07 and is identical to the result obtained from integrating the best-fit SED in Roccatagliata et al. (2009). Their fit implies that grains smaller than ~1 μm are responsible for the bulk of the infrared excess and that these grains reside at a minimum distance of 96 ± 23 AU from the central star. This minimum disk radius is consistent with the characteristic radius of 70 AU adopted in Equation (B1).

Since the collision time appears comparable to the time for the ISM to remove grains, we assume for our numerical models that a steady state is established in which the collisional generation of submicron grains within the posited birth ring is balanced by their removal by interstellar gas drag. We neglect the depletion of grains by collisions—this amounts to an order-unity error (see also Section 5.1, item 3). Within this framework, we follow the evolution of 10^5 0.1 μm particles. This single grain size is chosen for simplicity and is meant to be representative, given the polarization and color results described in Section 3. Based on the observed morphology, we choose an initial semi-major axis for all grains of 60 AU. Assuming that the observed grains are collisionally created by grains on circular orbits, Appendix A suggests the initial grain eccentricities can range from $e \sim 0$ to $e \sim 0.4$ for 0.1 μm grains, depending on the grain material and porosity. We adopt a representative value of $e = 0.2$ in our models, appropriate for moderately porous silicate grains. This eccentricity is consistent with the fractional ring width adopted in Equation (B1). We further choose random inclinations drawn from a uniform distribution extending from 0° to 10°, based on an assumed disk aspect ratio of $H/R \sim 0.1$, consistent with the system morphology in Figures 1 and 2 and with measurements of other highly inclined debris disks (Golimowski et al. 2006; Kalas 2005; Krist et al. 2005). Finally, we assume that the disk is initially circularly symmetric, such that the longitudes of

---

[10] This expression is equivalent to that given by Köhler & Mann (2004): $F_{\rm RP} = \int \frac{\pi a^2}{c} [Q_\nu^{\rm abs} + (1 - g_\nu) Q_\nu^{\rm sca}] F_\nu \, d\nu$.

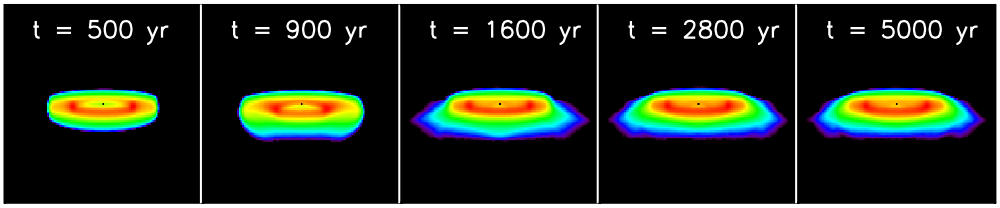

Figure 17. Five snapshots of an initially unperturbed, near edge-on disk subjected to interstellar gas drag from a warm, low-density cloud. The model assumes a steady state develops such that each time a grain is lost from the initially unperturbed ring, a new replacement grain is generated within the initial "birth ring." The relative flow direction in this example is coplanar with the disk midplane, and the equilibrated disk is equivalent to the third column in the first row of Figure 12. The observed morphology does not change after 3×10^3 years, setting the timescale for which the system is assumed to have achieved steady state.

ascending nodes, mean anomalies, and arguments of periastra are uniformly distributed between 0° and 360°.

Having chosen initial orbital elements, we next calculate the secular perturbations to the angular momentum and Runge–Lenz vectors, using the Scherer (2000) code base to average the Gaussian perturbation equations numerically over one orbit (Brouwer & Clemence 1961). We adopt an ISM density and encounter speed typical of warm interstellar clouds ($n_{\rm H\,I} = 0.2$ cm^{-3}, $v_{\rm rel} = 25$ km s^{-1}; Redfield 2006), though we note that the gas density is likely reduced by a factor a few inside the astrosphere relative to the nominal value outside (Bzowski et al. 2009). The direction of the flow vector relative to the disk has a significant effect on the resulting disk morphology, and we therefore test a range of flow directions.

To generate scattered-light images of the perturbed disk at some time after the initial encounter with the cloud, we calculate the classical elements from the resulting Runge–Lenz and angular momentum vectors and spread each grain over 100 points in its orbit in proportion to the time spent at each location. We estimate the equilibration timescale by monitoring the system morphology at successive times after the initial encounter with the cloud. Figure 17 shows an example of the disk morphology evolution for a highly inclined disk, 10° from edge-on. The relative flow direction in this example is coplanar with the disk midplane. The observed morphology does not change after 3×10^3 years, setting the timescale for which the system is assumed to have achieved steady state.

To create scattered light model images for comparison to HD 61005, we incline the equilibrated disk by 80° and −80°. We also generate model images inclined by 0° (face-on), 45°, 90° (edge-on), and −45° to illustrate the more general consequences of neutral gas drag. In our notation, positive inclinations indicate that the lower half of the disk in the image is closer to the observer than the upper half. The pixel size in our images is 2.6 AU, corresponding to the projected size of a NICMOS pixel ($0\farcs0759$) at the distance of HD 61005 (34.5 pc). The scattered light images also assume a Henyey–Greenstein phase function with a scattering asymmetry typical of debris disks ($g = 0.3$; Meyer et al. 2007). If the grains in HD 61005 are similar to those in AU Mic, as suggested by the color and polarization results (Section 3), a larger scattering asymmetry may be more appropriate (e.g., $g \sim 0.7$; Graham et al. 2007). However, the adopted scattering asymmetry has a relatively small effect on the qualitative morphology for highly inclined outer disks like HD 61005, as the majority of scattering angles present are near 90°.

The grid of models described above are shown in Figures 12–14. The image display scale is logarithmic, and each model is ≈310 AU (= 9″ for HD 61005) to a side. The labels at top indicate the disk inclination, and the labels at left indicate the azimuthal direction of the radial component of the flow vector. The bottom labels indicate the magnitude of the flow vector parallel and perpendicular to the disk midplane. The adopted coordinate system is illustrated with respect to the face-on disks in the left column of each Figure.

When a significant fraction of the relative flow vector is parallel to the disk midplane, Figures 12 and 13 show that a variety of morphologies can be produced, including bow structures ($i = 0°$), brightness asymmetries ($i = 80°, 90°, -80°$), and warps ($i = 90°/\theta = 0°$). As shown analytically by Scherer (2000) and discussed in Section 4.2.2, the neutral gas drag force acts to rotate the grain pericenters into a direction perpendicular to the flow vector, resulting in a buildup of particles in that direction. This effect is clearly observed in the face-on cases ($i = 0°$) in Figures 12 and 13.

For a highly inclined disk and a small range of radial flow directions ($\theta \sim 0°, 180°$), the models in Figures 12 and 13 show a swept morphology somewhat similar to HD 61005. This effect is produced both by the buildup of particles perpendicular to the flow vector and the non-zero inclination of the disk. Counterintuitively, the disk models with $v_r = 0$ and $v_z = |v|$ (Figure 14) do not show this structure and instead produce a largely symmetric distribution about the disk midplane. As discussed in Scherer (2000), this is because the direction in which a given grain's pericenter rotates to become perpendicular to the flow depends on the initial pericenter direction. As a result, grains with an initial direction to pericenter above the nominal midplane will persist in having a direction to pericenter at or above the midplane as long as they are bound to the star.

REFERENCES

Anderson, J., & King, I. R. 2000, PASP, 112, 1360
Anderson, J., & King, I. 2004, Multi-filter PSFs and Distortion Corrections for the HRC: ACS 2004-15 (Baltimore, MD: Space Telescope Science Institute)
Artymowicz, P., & Clampin, M. 1997, ApJ, 490, 863
Baraffe, I., Chabrier, G., Allard, F., & Hauschildt, P. H. 1998, A&A, 337, 403
Brouwer, D., & Clemence, G. M. 1961, Methods of Celestial Mechanics (New York: Academic)
Butler, R. P., Marcy, G. W., Williams, E., McCarthy, C., Dosanjh, P., & Vogt, S. S. 1996, PASP, 108, 500
Bzowski, M., Möbius, E., Tarnopolski, S., Izmodenov, V., & Gloeckler, G. 2009, Space Sci. Rev., 143, 177
Cappellari, M., & Copin, Y. 2003, MNRAS, 342, 345
Carpenter, J. M., et al. 2008, ApJS, 179, 423
Carpenter, J. M., et al. 2009, ApJS, 181, 197
Chiang, E., Kite, E., Kalas, P., Graham, J. R., & Clampin, M. 2009, ApJ, 693, 734
Cox, C., Ritchie, C., Bergeron, E., Mackenty, J., & Noll, K. 1997, NICMOS Distortion Correction–Instrument Science Report OSG-CAL-97-07 (Baltimore, MD: Space Telescope Science Institute)
D'Antona, F., & Mazzitelli, I. 1997, Mem. Soc. Astron. Ital., 68, 807
Debes, J. H., Weinberger, A. J., & Kuchner, M. J. 2009, ApJ, 702, 318
Dohnanyi, J. S. 1969, J. Geophys. Res., 74, 2531
Draine, B. T., & Lee, H. M. 1984, ApJ, 285, 89
Ferlet, R., Vidal-Madjar, A., & Gry, C. 1985, ApJ, 298, 838
Fitzgerald, M. P., Kalas, P. G., Duchêne, G., Pinte, C., & Graham, J. R. 2007, ApJ, 670, 536

Frisch, P. C., Grodnicki, L., & Welty, D. E. 2002, ApJ, 574, 834

Frisch, P. C. 2004, in AIP Conf. Proc. 719, Physics of the Outer Heliosphere, ed. V. Florinski, N. V. Pogorelov, & G. P. Zank (Melville, NY: AIP), 404

Gáspár, A., Su, K. Y. L., Rieke, G. H., Balog, Z., Kamp, I., Martínez-Galarza, J. R., & Stapelfeldt, K. 2008, ApJ, 672, 974

Golimowski, D. A., et al. 2006, AJ, 131, 3109

Graham, J. R., Kalas, P. G., & Matthews, B. C. 2007, ApJ, 654, 595

Gray, R. O., Napier, M. G., & Winkler, L. I. 2001, AJ, 121, 2148

Gray, R. O., Corbally, C. J., Garrison, R. F., McFadden, M. T., Bubar, E. J., McGahee, C. E., O'Donoghue, A. A., & Knox, E. R. 2006, AJ, 132, 161

Gunn, J. E., & Gott, J. R. I. 1972, ApJ, 176, 1

Heiles, C. 1997, ApJ, 481, 193

Heiles, C., & Troland, T. H. 2003, ApJ, 586, 1067

Hines, D. C., et al. 2007, ApJ, 671, L165

Holmberg, J., Nordstroem, B., & Andersen, J. 2008, VizieR Online Data Catalog, 5128, 0

Kalas, P., Graham, J. R., Beckwith, S. V. W., Jewitt, D. C., & Lloyd, J. P. 2002, ApJ, 567, 999

Kalas, P. 2005, ApJ, 635, L169

Kalas, P., Graham, J. R., Clampin, M. C., & Fitzgerald, M. P. 2006, ApJ, 637, L57

Kalas, P., Fitzgerald, M. P., & Graham, J. R. 2007, ApJ, 661, L85

Kenyon, S. J., & Bromley, B. C. 2004, AJ, 128, 1916

Köhler, M., & Mann, I. 2004, J. Quant. Spectrosc. Radiat. Transfer, 89, 453

Kozhurina-Platais, V., & Biretta, J. 2004, ACS/HRC Polarimetry Calibration III: Astrometry of the Polarized Filters: ACS 2004-11 (Baltimore, MD: Space Telescope Science Institute)

Krist, J. E., et al. 2005, AJ, 129, 1008

Krivov, A. V., Löhne, T., & Sremčević, M. 2006, A&A, 455, 509

Kruegel, E. 2003, in The Physics of Interstellar Dust, ed. E. Kruegel (IoP Series in Astronomy and Astrophysics; Bristol: Institute of Physics Publishing), ISBN 0750308613

Landgraf, M., Augustsson, K., Grün, E., & Gustafson, B. Å. S. 1999, Science, 286, 2319

Li, A., & Greenberg, J. M. 1998, A&A, 331, 291

Linde, T. J., & Gombosi, T. I. 2000, J. Geophys. Res., 105, 10411

Mann, I., Köhler, M., Kimura, H., Cechowski, A., & Minato, T. 2006, A&AR, 13, 159

Masana, E., Jordi, C., & Ribas, I. 2006, A&A, 450, 735

McKee, C. F., & Ostriker, J. P. 1977, ApJ, 218, 148

Meyer, D. M., Lauroesch, J. T., Heiles, C., Peek, J. E. G., & Engelhorn, K. 2006, ApJ, 650, L67

Meyer, D. M. 2007, in ASP Conf. Ser. 365, SINS—Small Ionized and Neutral Structures in the Diffuse Interstellar Medium, ed. M. Haverkorn & W. M. Goss (San Francisco, CA: ASP), 97

Meyer, M. R., Backman, D. E., Weinberger, A. J., & Wyatt, M. C. 2007, in Protostars and Planets V, ed. B. Reipurth, D. Jewitt, & K. Keil (Tucson, AZ: Univ. of Arizona Press), 573

Minato, T., Köhler, M., Kimura, H., Mann, I., & Yamamoto, T. 2006, A&A, 452, 701

Moro-Martin, A., Wyatt, M. C., Malhotra, R., & Trilling, D. 2008, in The Solar System Beyond Neptune, ed. A. Barucci (Tucson, AZ: Univ. Arizona Press), 465

Mouillet, D., Larwood, J. D., Papaloizou, J. C. B., & Lagrange, A. M. 1997, MNRAS, 292, 896

Müller, H.-R., Frisch, P. C., Florinski, V., & Zank, G. P. 2006, ApJ, 647, 1491

Nordström, B., et al. 2004, A&A, 418, 989

Perryman, M. A. C., et al. 1997, A&A, 323, L49

Pavlovsky, C. 2006, ACS Data Handbook, Version 5.0 (Baltimore, MD: Space Telescope Science Institute)

Redfield, S. 2006, in ASP Conf. Ser. 352, New Horizons in Astronomy: Frank N. Bash Symposium, ed. A. Frebel et al. (San Francisco, CA: ASP), 79

Redfield, S., & Linsky, J. L. 2008, ApJ, 673, 283

Roccatagliata, V., Henning, T., Wolf, S., Rodmann, J., Corder, S., Carpenter, J. M., Meyer, M. R., & Dowell, D. 2009, A&A, 497, 409

Scherer, K. 2000, J. Geophys. Res., 105, 10329

Schneider, G., et al. 2006, ApJ, 650, 414

Stanimirović, S., & Heiles, C. 2005, ApJ, 631, 371

Strubbe, L. E., & Chiang, E. I. 2006, ApJ, 648, 652

van Gorkom, J. H. 2004, in Clusters of Galaxies: Probes of Cosmological Structure and Galaxy Evolution, ed. J. S. Mulchaey, A. Dressler, & A. Oemler (Cambridge: Cambridge Univ. Press), 305

Vogt, S. S., et al. 1994, Proc. SPIE, 2198, 362

Wakker, B. P., & Mathis, J. S. 2000, ApJ, 544, L107

Warren, S. G. 1984, Appl. Opt., 23, 1206

Wehry, A., Krüger, H., & Grün, E. 2004, A&A, 419, 1169

Weidenschilling, S. J. 1977, MNRAS, 180, 57

Welsh, B. Y., Craig, N., Vedder, P. W., & Vallerga, J. V. 1994, ApJ, 437, 638

Wichmann, R., Schmitt, J. H. M. M., & Hubrig, S. 2003, A&A, 399, 983

Wood, B. E. 2004, Living Rev. Sol. Phys., 1, 2

Wyatt, M. C. 2008, ARA&A, 46, 339

Wood, B. E., Müller, H.-R., Zank, G. P., Linsky, J. L., & Redfield, S. 2005, ApJ, 628, L143